Petroleum Science 23 (2026) 6960–6978

Contents lists available at ScienceDirect

Petroleum Science

journal homepage: www.keaipublishing.com/en/journals/petroleum-science

Original Paper

Microscale occurrence and adsorption behavior of pore water in shale oil reservoirs: Insights from water vapor adsorption at varying relative humidities

Wei-Zheng Gao [a,b], Peng-Fei Zhang [a,b,*], Jun-Jie Wang [a,b], Hai-Yong Wang [c], Neng-Wu Zhou [a,b], Wen-Biao Li [a,b], Guo-Hui Chen [a,b], Chen-Xi Wu [a,b], Shuang-Fang Lu [a,b,**]

[a] Sanya Offshore Oil & Gas Research Institute of Northeast Petroleum University, Sanya, 572025, Hainan, China
[b] State Key Laboratory of Continental Shale Oil, Northeast Petroleum University, Daqing, 163318, Heilongjiang, China
[c] Exploration & Development Research Institute of Daqing Oilfield Company Ltd. PetroChina, Daqing, 163712, Heilongjiang, China

ARTICLE INFO

Article history:
Received 2 September 2025
Received in revised form
24 January 2026
Accepted 19 July 2026
Available online 23 July 2026

Edited by Xiu-Fang Hu

Keywords:
Water vapor adsorption
Low-temperature nitrogen adsorption–desorption
Microscopic pore structure
Shale oil reservoir
Gulong Sag

ABSTRACT

The water saturation in shale reservoirs plays a key role in controlling shale oil accumulation and production. The microscale distribution of pore water constrains both the content and spatial occurrence of adsorbed and free oil. Therefore, investigating the occurrence characteristics of pore water in shale oil reservoirs is essential for understanding the mechanisms of oil–water interactions. In this work, the shales from the Qingshankou Formation in the Gulong Sag were selected. Water vapor adsorption experiments were conducted under controlled relative humidities of 23%, 33%, 56%, 75%, 85%, and 98%. At each relative humidity (RH), low-temperature nitrogen adsorption tests were conducted to monitor the evolution of pore structure during water vapor adsorption. Subsequently, changes in pore-scale heterogeneity and the factors controlling water adsorption were analyzed. The results show that the Dent model effectively distinguishes between primary adsorption, occurring at specific adsorption sites, and secondary adsorption among water molecules, corresponding to Type I and Type III isotherms, respectively. At low RH, water vapor adsorption is dominated by primary adsorption, forming a monolayer. As RH increases, secondary adsorption becomes dominant, resulting in multilayer formation, and at high RH, capillary condensation prevails. Nitrogen adsorption data indicated that increasing RH reduced the BET specific surface area (SSA) and pore volume (PV), whereas average pore diameter (APD) increased. Multifractal parameters ΔD and $D_{-10}-D_0$ decreased with increasing RH. At low RH, larger micro- and mesopore volumes were more strongly affected by water vapor adsorption, leading to more uniform pore filling and reduced heterogeneity. In contrast, the D_0-D_{10} increased with increasing RH, especially when RH exceeded 85%, reflecting the influence of capillary condensation within macropores. Clay mineral content significantly influenced adsorption, particularly under low RH. TOC exhibited a similar trend, likely due to organo-clay complex pore-fractures. PV and BET SSA similarly influenced adsorption, with notable effects mainly at low RH. These insights are expected to elucidate the microscale occurrence mechanisms of pore water within the complex pore–fracture system of shale, and provide a basis for understanding oil–water distribution and interactions in shale oil reservoirs.

© 2026 The Authors. Publishing services by Elsevier B.V. on behalf of KeAi Communications Co. Ltd. This is an open access article under the CC BY license (http://creativecommons.org/licenses/by/4.0/).

1. Introduction

As a critical alternative energy source to conventional oil, shale oil has garnered significant attention because of its substantial reserves (Zou et al., 2019; Jin et al., 2021; Li et al., 2024). Recent years have witnessed considerable advancements in shale oil exploration and development across multiple basins in China,

* Corresponding author.
** Corresponding author.
E-mail addresses: zhangpengfei@nepu.edu.cn (P.-F. Zhang), lushuangfang@nepu.edu.cn (S.-F. Lu).

Peer review under the responsibility of China University of Petroleum (Beijing).

https://doi.org/10.1016/j.petsci.2026.07.037
1995-8226/© 2026 The Authors. Publishing services by Elsevier B.V. on behalf of KeAi Communications Co. Ltd. This is an open access article under the CC BY license (http://creativecommons.org/licenses/by/4.0/).

accompanied by a notable growth in production. However, the implementation of efficient and sustainable recovery strategies remains technically challenging (Sun et al., 2021; Xi et al., 2023; Zhang et al., 2023; Li et al., 2024; Wang et al., 2024a). A critical constraint lies in the complex subsurface environment, where shale oil coexists with formation water within intricate pore-fracture systems. The water content within these reservoirs exhibits significant variability, controlled by basin-specific geological settings and thermal maturity (Cheng et al., 2019; Zhang et al., 2025). Fundamentally, water saturation governs oil occurrence, as formation water competes for storage space within the pore network, which in turn controls shale oil accumulation and producibility (Yang et al., 2020).

Current research on pore water in shale has predominantly focused on highly mature shale gas reservoirs, while studies concerning the occurrence characteristics and controlling factors of liquid-phase pore water in shale oil reservoirs remain limited (Li et al., 2019; Wang et al., 2019a; Bai et al., 2020; Yang et al., 2020; Xie et al., 2023). Generally, compared to shale gas reservoirs, shale oil reservoirs are characterized by relatively lower thermal maturity and a pore system dominated by inorganic minerals, distinct from the organic matter (OM) pores prevalent in gas reservoirs. In particular, the relatively higher content of clay minerals provides a vast specific surface area that profoundly impacts water vapor adsorption (Zhang et al., 2024). Consequently, unlike gas residing in hydrophobic OM pores, shale oil often competes directly with water for occupancy in hydrophilic or mixed-wet inorganic pores. Numerous Nuclear Magnetic Resonance (NMR) studies have corroborated this, indicating that capillary-bound water coincides with adsorbed oil space, while mobile water shares space with capillary-bound oil (Gao et al., 2025; Wang et al., 2025). Therefore, variations in pore water content inevitably induce reconfiguration of the occurrence state of pore oil.

Previous studies have demonstrated that water adsorption mechanisms in shale are highly sensitive to ambient relative humidity (RH). It typically follows a transition from monolayer to multilayer adsorption at low RH, culminating in capillary condensation within pore structures at high RH (Sang et al., 2019; Lahn et al., 2020; Qin et al., 2024). This process is governed by mineralogical composition and pore structure, ultimately leading to alterations in pore heterogeneity (Hatch et al., 2012; Wang et al., 2019a; Xie et al., 2023). It is generally accepted that inorganic minerals are hydrophilic, while organic matter (OM) exhibits hydrophobicity (Sulucarnain et al., 2012; Korb et al., 2014; Li et al., 2018; Chen et al., 2019). Hydrophilic clay minerals, characterized by polar functional groups and exchangeable cations, are the primary control on water vapor adsorption, exhibiting a strong positive correlation with both adsorption capacity and rate (Zolfaghari et al., 2017a, 2017b). Additionally, pore structure critically limits adsorption capacity; while high specific surface areas in micro- and nanopores promote uptake, limited pore volume (PV) can restrict further accumulation under high RH conditions (Li et al., 2016b; Bai et al., 2020).

To quantitatively describe these complex adsorption processes, several thermodynamic models have been developed. The Langmuir isotherm describes monolayer adsorption (Langmuir, 1918), while the BET isotherm accounts for multilayer adsorption (Brunauer et al., 1938), and the GAB model, which accounts for adsorption heat variations beyond the first layer, has been widely applied to minerals such as montmorillonite and illite (Feng et al., 2018). Building on these theories, the Dent multilayer adsorption model is commonly used to characterize water vapor adsorption on shale pore surfaces. Its advantage lies in its ability to distinguish between primary (strongly bound) and secondary (weakly bound) adsorption layers, providing a theoretical basis for differentiating water occurrence states within the pore network (Wang et al., 2019a; Bai et al., 2020; Xie et al., 2023).

However, while thermodynamic models are effective in evaluating water adsorption mechanisms and quantifying uptake capacity, they fail to capture the dynamic physical alteration of the pore structure induced by this process. Previous studies have noted that water adsorption behaviors vary among pore types in shale gas reservoirs (Bai et al., 2020; Xie et al., 2023; Xing et al., 2025), yet the dynamic change of this process on the residual pore structure has been insufficiently evaluated. Furthermore, research into water adsorption and these pore structure dynamic changes in high-clay shale oil reservoirs is even more limited. To address this, shale samples from the K_2qn in the Gulong Sag, representing a typical continental shale rich in clay minerals and micropores, were systematically investigated (Sun et al., 2021; He et al., 2023). Water vapor adsorption experiments under varying RH were conducted, combined with low-temperature nitrogen adsorption/desorption (LTNA/D) tests and scanning electron microscopy (SEM) observations. The relationships between water vapor adsorption capacity, mineral composition, and pore structure under different RH were analyzed. Furthermore, the evolution of pore heterogeneity and its controlling factors were discussed. These findings contribute to a deeper understanding of pore water adsorption behavior within multiscale pore networks of continental shale reservoirs and provide insights into the mechanisms governing oil–water occurrence in shale oil reservoirs.

2. Geological setting

The Songliao Basin, located in northeastern China, covers an area of about 26×10^4 km^2 and hosts abundant hydrocarbon resources. It exhibits a NE-trending orientation and displays a two-tiered architecture comprising an early-stage fault depression overlain by a later depression (Fig. 1(a)), representing a classic superimposed rift-depression basin (Wang et al., 2013). Shale deposition in the Songliao Basin primarily occurred during the Cretaceous period, associated with two major lacustrine transgression events. These sediments were deposited in deep to semi-deep lacustrine environments, resulting in the accumulation of thick, organic-rich dark mudstones within the Qingshankou (K_2qn) and Nenjiang (K_2n) formations. Compared with the K_2n shale, the K_2qn shale is characterized by higher total organic carbon (TOC) content and greater thermal maturity, and currently represents the principal reservoir interval for Gulong shale oil (Jia et al., 2013; Xu et al., 2015; Liu et al., 2017). The Qijia Gulong Sag, Daqing Placanticline, and Sanzhao Sag, located within the Central Depression, are characterized by relatively rich shale oil resources (Fig. 1(b) and (c)), with the Gulong Sag being the primary exploration target. Stratigraphically, the K_2qn in the Gulong sag is subdivided into the first member (K_2qn^1) and the second to third members (K_2qn^{2+3}), with the K_2qn^1 and the lower intervals of K_2qn^{2+3} exhibiting significant potential for exploration and development (Sun et al., 2021; Zhang et al., 2023).

3. Materials and methods

3.1. Samples

A total of seven shale samples were collected from the K_2qn in Well A1, located in the Gulong Sag, with sampling depths ranging from 2332.76 m to 2439.25 m (Fig. 1(c) and (d)). Specifically, the

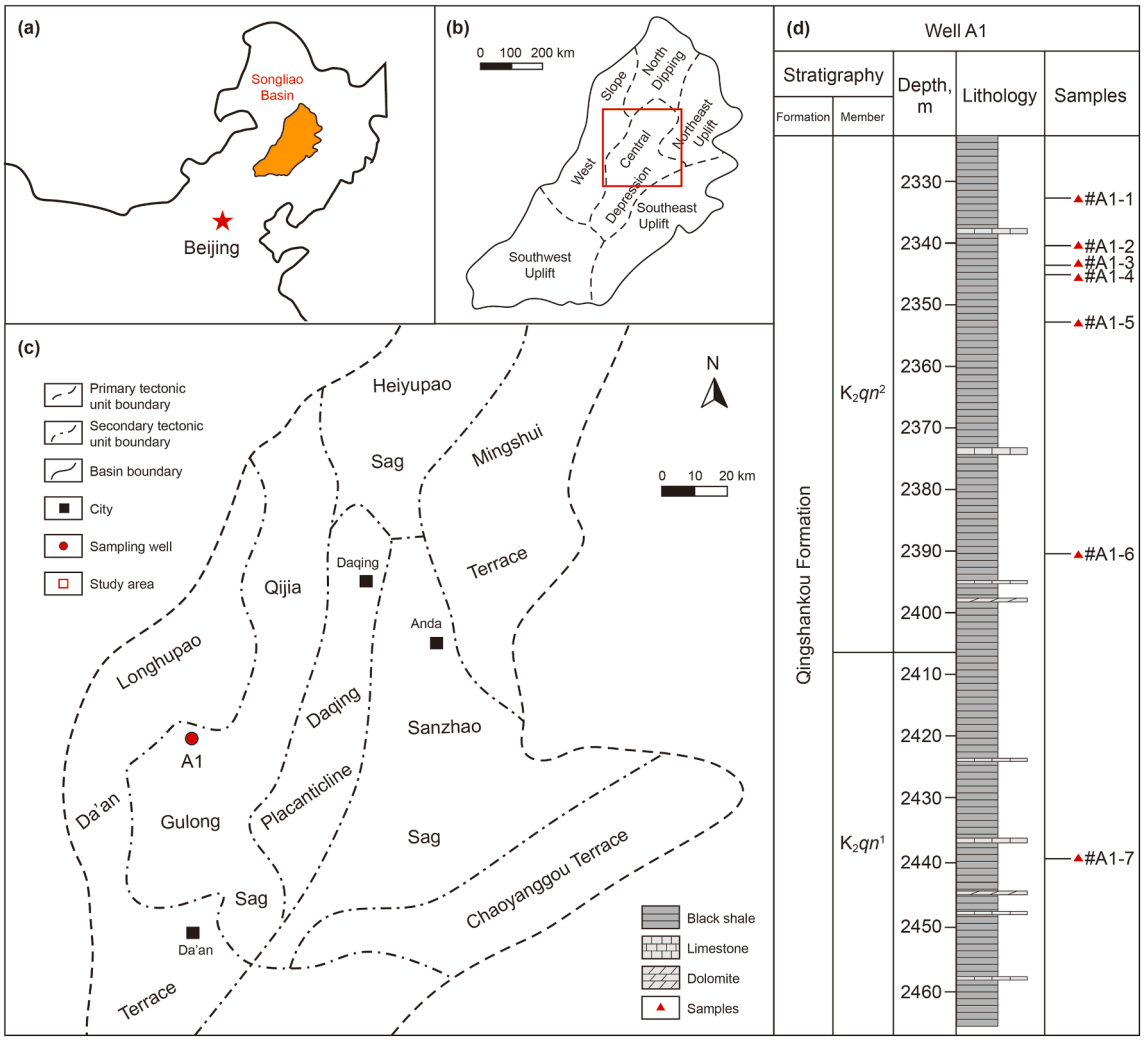


Fig. 1. Locations of the Songliao Basin in northeastern China **(a)**, the Central Depression **(b)**, and the sampling well **(c)**. Stratigraphic column and the sampling positions in Well A1 **(d)**.

Table 1
Basic parameters summary of selected shales.

Sample	Depth, m	Formation	R_o, %	TOC, %	Mineral composition, %					Clay minerals, %		
					Q	Pl	Ca	D	Cl	I	Ch	I/S
A1-1	2332.76	K_2qn^2	1.23	2.06	37.8	22.7	/	/	34.6	66	8	26
A1-2	2340.75	K_2qn^2	1.24	2.84	35.3	22.5	/	2.9	35.0	58	15	27
A1-3	2344.80	K_2qn^2	1.25	2.09	35.6	29.5	1.1	/	29.6	72	7	21
A1-4	2345.58	K_2qn^2	1.25	1.89	35.0	27.3	0.9	/	32.9	71	8	21
A1-5	2353.98	K_2qn^2	1.26	1.78	35.2	30.4	1.5	/	29.3	63	16	21
A1-6	2390.25	K_2qn^2	1.30	2.11	34.5	20.5	0.8	/	39.4	57	11	32
A1-7	2439.25	K_2qn^1	1.37	3.27	36.7	10.3	4.4	/	48.6	49	25	26

Note: The symbol "/" indicates that it has not been detected. Q, Pl, Ca, D, Py, Cl, I, Ch, and I/S are the quartz, plagioclase, calcite, dolomite, pyrite, clay minerals, illite, chlorite, and mixed-layer illite/smectite, respectively.

sample set comprises one sample from K_2qn^1 and six from K_2qn^2, characterized by similar mineralogy but distinct TOC levels (Table 1). The primary experiments comprised SEM, water vapor adsorption experiments, and corresponding LTNA/D tests, aimed at elucidating the mechanisms of water vapor uptake and the associated changes in pore structure. The Dent model was applied to characterize the water vapor adsorption mechanisms, and multifractal theory was employed to investigate variations in pore structure heterogeneity.

3.2. Experimental procedures

The detailed experimental procedures are illustrated in Fig. 2. Upon receipt, each original sample was cut into a cylindrical plug with a diameter of approximately 25 mm. A thin disc (2–3 mm in thickness) was then sliced from the end of each plug. The remaining rock fragments and offcuts produced during the wire-cutting process were collected and ground into powders with a particle size of 40–60 mesh (0.25–0.42 mm). Subsequently, solvent

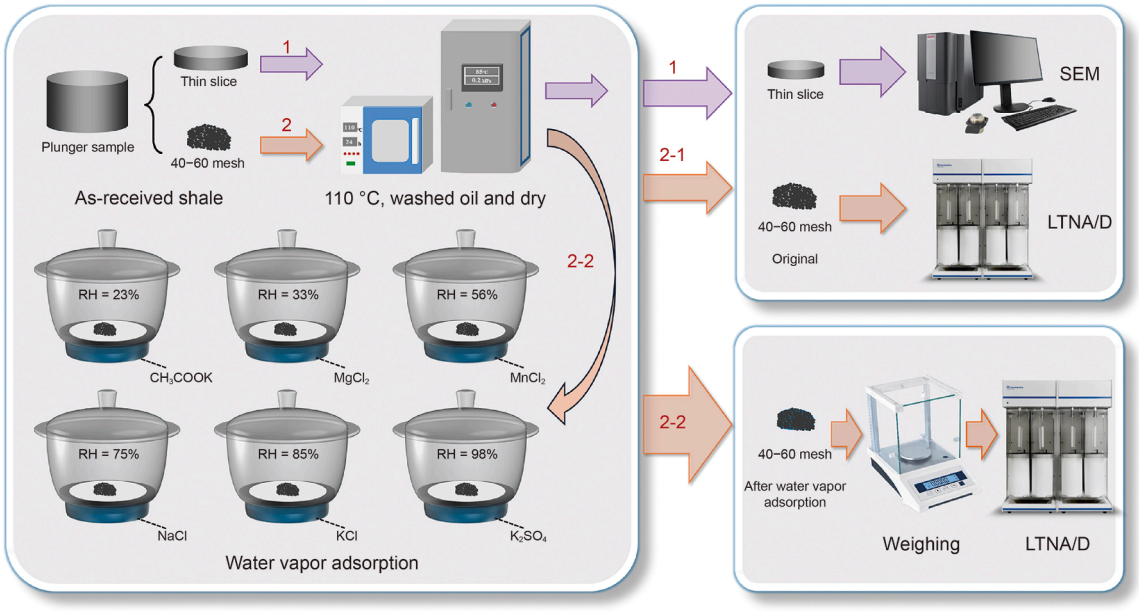


Fig. 2. Schematic diagram of the experimental setup and procedures.

extraction and drying treatments were performed (Processes 1 and 2). Specifically, a mixture of dichloromethane and acetone (volume ratio 3:1) was used to extract residual hydrocarbons under conditions of 85 °C and 0.2 MPa for 7 days. The samples were subsequently vacuum-dried at 110 °C for 24 h and then transferred to a desiccator to cool to ambient temperature (25 °C) (Wang et al., 2024b; Gao et al., 2025). The polished end surfaces were then subjected to analysis using a Phenom ProX SEM system to obtain representative micrographs of each sample. Detailed specifications of the equipment are available in previous research (Gao et al., 2025). The solvent-extracted and dried powders were equally divided into seven portions by mass. One portion was directly analyzed by nitrogen adsorption to characterize the original pore structure parameters (Process 2-1). The remaining six portions were equilibrated under different RH conditions. After reaching mass stability, nitrogen adsorption experiments were conducted under each RH condition to assess the corresponding pore structure characteristics (Process 2-2).

3.2.1. Scanning electron microscopy (SEM) test

Before the SEM experiment, cuttings were first manually polished and then finished by argon-particle polishing. Imaging was carried out with a Phenom ProX SEM (maximum magnification 12,000×); routine observations were made at 4000×, yielding an approximate resolution of 32 nm (Gao et al., 2025).

3.2.2. Water vapor adsorption experimental process

The detailed procedure for the water vapor adsorption equilibrium experiment is as follows:

(a) The solvent extraction and drying process of the powdered shale samples followed the methodology previously described. This step was conducted to ensure the complete removal of pore fluids from the shale matrix.
(b) To establish environments with controlled RH, six saturated salt solutions were prepared, corresponding to target RH values of 23%, 33%, 56%, 75%, 85%, and 98%. These levels were achieved using CH_3COOK, $MgCl_2$, $MnCl_2$, NaCl, KCl, and K_2SO_4, respectively (Feng et al., 2018; Shen et al., 2018; Zhang et al., 2025). The samples were placed in a sealed chamber (Fig. 2), and all adsorption procedures were carried out at a constant temperature of 25 °C to ensure thermal stability.
(c) Once placed in the chamber, the samples were weighed every 12 h to record mass changes. Equilibrium was considered to be reached when the rate of mass change was less than 0.1%. A high-precision balance with an accuracy of 0.1 mg was employed to record mass variations at each stage. To minimize the influence of ambient humidity during weighing, samples were returned to the RH-controlled chamber immediately after measurement and allowed to re-equilibrate for 24 h before nitrogen adsorption analysis.

3.2.3. Low-temperature nitrogen adsorption–desorption (LTNA/D)

The LTNA/D tests were performed on shales in dry and water vapor adsorption equilibrium states. Following the completion of water vapor adsorption equilibrium, the samples equilibrated under different RH were allowed to stand in the sealed chamber for an additional 24 h before proceeding with LTNA/D analyses. These measurements were performed using a Micromeritics ASAP 2460 surface area and porosity analyzer. Nitrogen adsorption and desorption isotherms were obtained at 77 K over a relative pressure range of 0.01 to 0.993. Note that before testing, samples at different RH require humidity-equilibrated powder to be placed in liquid nitrogen (77K) to solidify the water content within the shale. Subsequently, the frozen powder is evacuated for 1 h before conducting the LTNA/D test. The specific surface area (SSA) was calculated using the Brunauer–Emmett–Teller (BET) model (BET SSA), while the pore size distribution (PSD) was derived from the desorption branch of the isotherms using the Barrett–Joyner–Halenda (BJH) method (Zhang et al., 2019; Wang et al., 2025).

3.3. Methodologies

3.3.1. Dent model of water vapor adsorption

Water vapor adsorption in shale involves a combination of physical and chemical mechanisms. The distribution and retention of water molecules within organic and inorganic pores under

varying RH can significantly influence the occurrence and mobility of shale oil. Building on previous work related to adsorption modeling, the Dent multilayer adsorption model was developed based on Langmuir theory and modified BET approaches to describe the interaction of water vapor with shale pore surfaces (Dole, 1948; Dent, 1977; Charrière and Behra, 2010). This model incorporates two types of adsorption sites: primary (Q_1) and secondary (Q_2) (Wang et al., 2019a; Dang et al., 2021). The primary sites, associated with monolayer adsorption, are mainly controlled by pore diameter and surface chemical properties, and are typically linked to clay minerals with high water affinity. Water molecules at these sites are directly bound to the pore surface, exhibiting relatively high binding energies. In contrast, secondary sites represent multilayer adsorption and capillary condensation processes, primarily influenced by PV and the presence of weakly interactive or hydrophobic pore surfaces, where water molecules exhibit lower binding energies (Zolfaghari et al., 2017a; Bai et al., 2020).

Accordingly, under the assumption of a porous system with dual adsorption sites and BET-type multilayer adsorption, the Dent model is expressed in detail as follows:

$$Q(\mathrm{RH}) = \frac{w_\mathrm{m} \times K_1 \times \mathrm{RH}}{(1 - K_2 \times \mathrm{RH})(1 - K_2 \times \mathrm{RH} + K_1 \times \mathrm{RH})} \tag{1}$$

$$Q(\mathrm{RH}) = \frac{m_\mathrm{RH} - m_\mathrm{Dry}}{m_\mathrm{Dry}} \tag{2}$$

where Q(RH) represents the specific amount of water vapor adsorbed at a given RH, g/g, and is calculated using Eq. (2). w_m denotes the maximum adsorption capacity per unit mass of the sample. K_1 and K_2 constants corresponding to the adsorption affinities of primary and secondary sites, respectively, are dimensionless; larger K values indicate stronger adsorption capabilities. m_RH is the mass of the sample after water adsorption under a specific RH condition, g, while m_Dry refers to the dry weight of the sample, g.

According to the Dent model, as RH increases, the adsorption capacities at primary and secondary sites can be derived from the classical Dent formulation, where Q_1 and Q_2 are described by Eqs. (3) and (4). The parameters w_m, K_1, and K_2 are determined by fitting Eq. (1) to the experimental data:

$$Q_1 = \frac{w_m \times K_1 \times \mathrm{RH}}{1 + \mathrm{RH} \times (K_1 - K_2)} \tag{3}$$

$$Q_2 = \frac{w_m \times K_1 \times K_2 \times \mathrm{RH}^2}{(1 - K_2 \times \mathrm{RH})[1 + (K_1 - K_2) \times \mathrm{RH}]} \tag{4}$$

3.3.2. Fractal analysis

The study of shale heterogeneity is essential to understanding the complexity of pore structures in porous media (Wang et al., 2025). In highly heterogeneous shale reservoirs, the PSD often exhibits significant fluctuations. Under such conditions, single fractal models often fail to describe the variability in pore size heterogeneity adequately (Liu et al., 2018). Multifractal theory offers distinct advantages in characterizing the heterogeneity of unconventional reservoir pores and is now widely employed in fractal-based analyses of shale pore structures (Hou et al., 2020; Zhang et al., 2022; Yao et al., 2024). The multifractal spectrum is typically expressed in two fundamental forms: the α–$f(\alpha)$ singularity spectrum and the q–$D(q)$ generalized fractal dimension spectrum. These two spectra respectively characterize local heterogeneity and information-theoretic scaling behavior of multifractals. A significant linear relationship has been reported between them in previous studies. Therefore, the q–$D(q)$ spectrum was adopted to quantify multifractal properties in this study. Its mathematical definition is provided in Eq. (5):

$$D(q) = \frac{\tau(q)}{q - 1} \tag{5}$$

where $D(q)$ denotes the generalized fractal dimension spectrum, q is the order of the statistical moment, and $\tau(q)$ represents the quality index function.

When $q = 1$, the calculation formula for $D(q)$ becomes:

$$D_1 = \lim_{\varepsilon \to 0} \frac{\sum_{i=1}^{N(\varepsilon)} P_i(\varepsilon) \times \log P_i(\varepsilon)}{\log \varepsilon} \tag{6}$$

The $D(q)$ reflects the scaling behavior of PV distribution at different moment orders, while D corresponds to the information dimension. Specifically, the difference D_{-10}–D_0 characterizes the heterogeneity associated with low PV, D_0–D_{10} reflects the heterogeneity in regions of high PV, and D_{-10}–D_{10} quantifies the overall PV heterogeneity within the sample (Zhang et al., 2022; Yao et al., 2024).

4. Results

4.1. Characteristics of selected shales

4.1.1. R_o, TOC, and mineral compositions of selected shales

All samples exhibit relatively high TOC contents, varying between 1.77% and 3.27%, with an average of 2.23%. And they also display relatively high maturity, with R_o values showing an average of approximately 1.27%. The mineralogical composition is broadly consistent across the samples, indicating lithological homogeneity. The dominant constituents are clay minerals (average 35.63%) and quartz (average 35.73%). Within the clay fraction, illite is the most abundant, accounting for 49% to 72% (mean 62.38%). Plagioclase is present in moderate amounts, while carbonate minerals are present in extremely low abundance or absent in some samples (Table 1).

4.1.2. Pore types of selected shales

Two primary types of pore structures occurred in the shale samples from the study area: intragranular and intergranular pores, with the former being more prevalent. Intragranular pores are predominantly associated with clay minerals. Clay minerals are dominated by illite, which commonly occurs as flocculent aggregates and is characterized by the development of thin, sheet-like, and slit-shaped intragranular pores, and the irregular slit pores are mainly related to organo-clay complex pore-fractures (Sun et al., 2024) (Fig. 3(c), (e), and (f)). In addition, dissolution pores were observed within plagioclase grains (Fig. 3(d)), and cleavage fractures were occasionally noted in plagioclase (Fig. 3(b)). In contrast, intergranular pores are relatively scarce and are mainly developed at grain boundaries around quartz particles (Fig. 3(a), (c), and (e)). Quartz grains are generally larger and frequently encapsulated by clay minerals, which limits interparticle pore space. Pyrite aggregates were also observed, displaying intercrystalline pores (Fig. 3(a) and (b)).

4.2. Water vapor adsorption isotherms

All samples exhibited a good fit with the Dent model. According to the Brunauer classification of adsorption isotherms (Brunauer et al., 1938), the water vapor adsorption isotherms of all samples

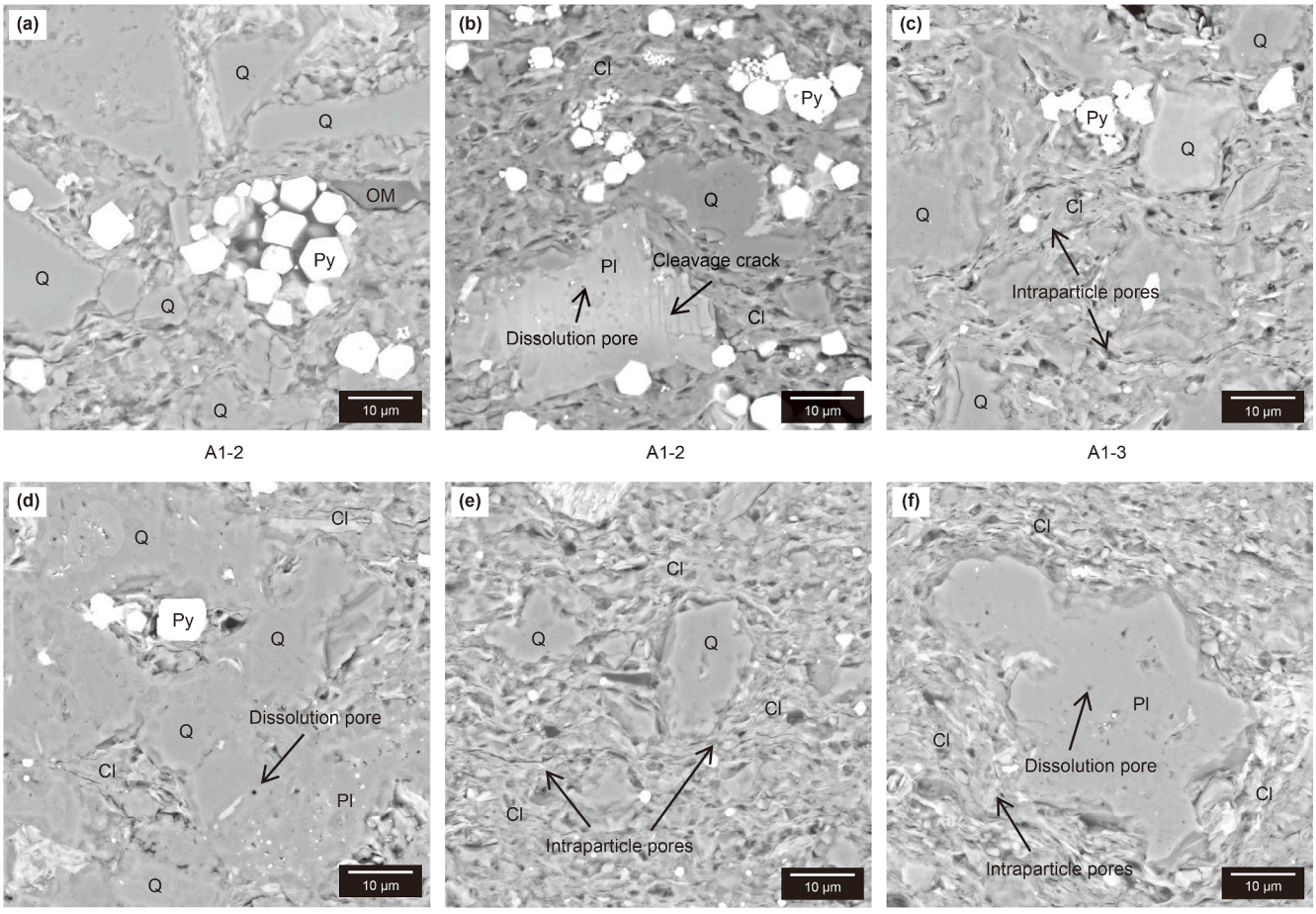


Fig. 3. Pore types in the selected shales by SEM images. Cl, clay minerals; OM, organic matter; Pl, plagioclase; Py, pyrite; Q, quartz.

correspond to Type II isotherms (Fig. 4), indicating the coexistence of monolayer adsorption, multilayer adsorption, and capillary condensation within the multiscale pore networks of the shale matrix. This is similar to previous studies on the shales of the Wufeng–Longmaxi Formation (Wang et al., 2019a; Xie et al., 2023; Zhang et al., 2025). The fitted model parameters are summarized in Table 2. The values of K_1 and K_2 range from 1.85 to 8.70 (average 4.00) and from 0.55 to 0.70 (average 0.61), respectively, suggesting that the adsorption strength of primary adsorption is significantly higher than that of secondary adsorption. No clear correlation was observed between w_m and either K_1 or K_2, indicating that these constants characterize the adsorption strength rather than the amount adsorbed.

Based on the fitted values, the isotherms for primary and secondary adsorption were derived. The primary adsorption isotherms correspond to the Type I isotherm as classified by IUPAC, predominantly governed by monolayer adsorption. These isotherms exhibit an upward-convex shape, with adsorption capacity increasing rapidly at low RH and leveling off as RH exceeds approximately 0.3. In contrast, secondary adsorption isotherms differ markedly from the primary ones and align with the Type III IUPAC classification. These isotherms are downward-concave, indicating that multilayer adsorption dominates the process. At low RH, the adsorption capacity increases slowly, but at higher RH, it rises sharply and tends toward capillary condensation. An intersection between the primary and secondary adsorption isotherms is observed for all samples, beyond which the amount of secondary adsorption becomes predominant. Notably, the location of this crossover varies among samples, reflecting differences in mineral composition and pore structure that affect water vapor adsorption behavior. In contrast to the Longmaxi Formation, no significant capillary condensation was detected at high RH in the present samples, as indicated by the lack of a distinct upward inflection in the isotherms. This phenomenon may be attributed to mineralogical differences: the studied shales are predominantly clay-rich, whereas the Longmaxi Formation contains less than 10% clay minerals on average and is largely composed of brittle minerals (average 88.3%) (Bai et al., 2020).

The primary and secondary adsorption capacities at different RH were obtained from the corresponding isotherms (Table 3). At an RH of 23%, primary adsorption exhibited a marked increase, with a relatively high average value of 8.18×10^{-3} g/g, whereas secondary adsorption remained low, averaging only 1.35×10^{-3} g/g. When RH increased to 33%, both primary and secondary adsorption showed limited changes, with average values of 9.92×10^{-3} g/g and 2.53×10^{-3} g/g, respectively. As RH continued to rise, the increment in primary adsorption gradually diminished. The mean primary adsorption values at 56%, 75%, 85%, and 98% RH were 12.55×10^{-3} g/g, 13.95×10^{-3} g/g, 14.53×10^{-3} g/g, and 15.15×10^{-3} g/g, respectively, indicating a trend toward saturation. In contrast, secondary adsorption demonstrated a substantial and continuous increase across the same RH range, with corresponding average values of 6.58×10^{-3} g/g, 11.91×10^{-3} g/g, 15.88×10^{-3} g/g, and 23.06×10^{-3} g/g. This divergent behavior highlights the distinct

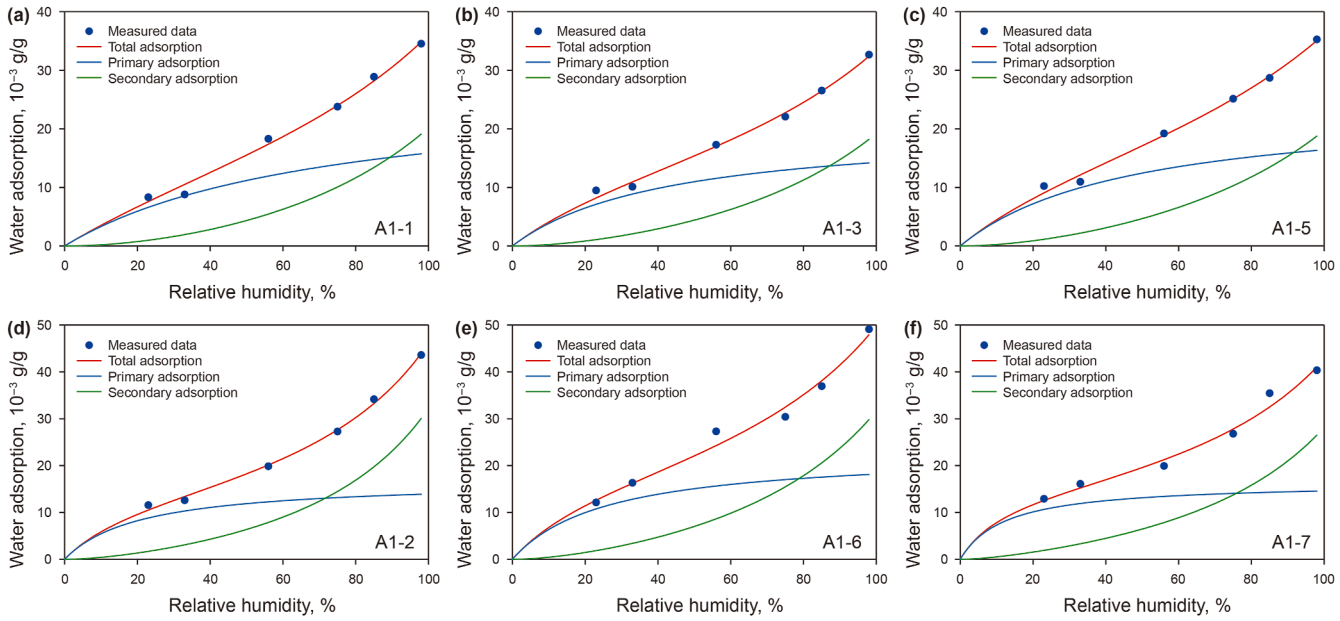


Fig. 4. Water vapor adsorption isotherms. **(a)**–**(f)** The clay mineral contents are 34.6%, 29.6%, 32.9%, 35.0%, 39.4%, and 48.6%, respectively.

Table 2
Fitting parameters and results of the Dent model.

Samples	K_1	K_2	w_m, g/g	R^2
A1-1	1.941	0.560	0.0195	0.9946
A1-2	5.462	0.698	0.0147	0.9978
A1-3	2.902	0.574	0.0164	0.9961
A1-4	1.849	0.598	0.0164	0.9747
A1-5	2.662	0.546	0.0192	0.9967
A1-6	4.481	0.635	0.0197	0.9899
A1-7	8.702	0.659	0.0152	0.9887

moisture uptake mechanisms between primary and secondary adsorption processes under elevated humidity conditions.

4.3. Changes in multiscale pore structure and heterogeneity after water vapor adsorption

4.3.1. Pore structure parameters of original shale

The original nitrogen adsorption–desorption isotherms of all shale samples are presented in Fig. 5. According to the IUPAC classification, the isotherms correspond to Type II, indicating the presence of monolayer adsorption, multilayer adsorption, and capillary condensation. A distinct hysteresis loop is observed between the adsorption and desorption branches. The selected shales exhibit H2–H3 type hysteresis behavior (Fig. 5(a)), suggesting the coexistence of ink-bottle-shaped pores and slit-like pores. The pore size distributions (PSDs) of all samples display a bimodal pattern. The first peak, which is more pronounced, appears around 3 nm, indicating the dominance of micropores or narrow mesopores. The second, broader and lower peak is centered around 30–40 nm, reflecting the development of wider mesopores.

4.3.2. Changes in shale pore structure of LTNA/D

Low-temperature nitrogen adsorption/desorption (LTNA/D) tests on moisture-equilibrated shales are commonly employed to evaluate the effects of moisture on microscopic pore structures (Chen et al., 2021b; Xie et al., 2023; Zhang et al., 2025). Water vapor adsorption on shale surfaces gradually increases with increasing RH, accompanied by notable changes in the nitrogen adsorption–desorption isotherms. A pronounced decrease in nitrogen adsorption capacity is observed with rising RH, particularly from the dry state to 23% RH, indicating that water vapor significantly adsorbs onto the pore surfaces and competitively inhibits nitrogen uptake (Fig. 6). In addition, a distinct transition in hysteresis loop type occurs between 33% and 56% RH, shifting from H2–H3 to H3-type behavior. This change suggests a transition from the coexistence of ink-bottle-shaped and slit-like pores to a pore system dominated primarily by slit-like geometries (Fig. 6). This phenomenon implies that water vapor preferentially occupies ink-bottle-shaped micropores during this humidity interval. Such

Table 3
Adsorption content of water vapor under different RH of selected shales.

Sample	Water vapor adsorption capacity, 10^{-3} g/g					
	23%	33%	56%	75%	85%	98%
A1-1	7.57[a] (6.60[b], 0.97[c])	10.51 (8.57, 1.94)	17.38 (11.93, 5.45)	23.99 (13.92, 10.07)	28.17 (14.77, 13.40)	34.84 (15.73, 19.11)
A1-2	10.50 (8.81, 1.69)	13.39 (10.30, 3.08)	20.13 (12.26, 7.87)	27.64 (13.17, 14.47)	33.25 (13.52, 19.73)	43.95 (13.88, 30.07)
A1-3	8.19 (7.11, 1.08)	10.93 (8.86, 2.07)	17.00 (11.54, 5.46)	22.76 (12.97, 9.79)	26.44 (13.55, 12.89)	32.39 (14.18, 18.21)
A1-4	6.27 (5.41, 0.86)	8.81 (7.07, 1.74)	15.00 (9.97, 5.03)	21.26 (11.72, 9.54)	25.39 (12.47, 12.91)	32.24 (13.33, 18.91)
A1-5	9.05 (7.92, 1.14)	12.13 (9.94, 2.18)	18.89 (13.12, 5.77)	25.12 (14.84, 10.28)	28.99 (15.54, 13.45)	35.08 (16.32, 18.76)
A1-6	12.59 (10.75, 1.84)	16.20 (12.81, 3.40)	24.27 (15.64, 8.63)	32.47 (17.00, 15.46)	38.10 (17.53, 20.57)	47.92 (18.1, 29.83)
A1-7	12.54 (10.64, 1.90)	15.21 (11.91, 3.31)	21.26 (13.41, 7.84)	27.80 (14.06, 13.74)	32.50 (14.3, 18.20)	41.06 (14.55, 26.51)

Note: a, b, and c refer to the total adsorption capacity, primary adsorption capacity, and secondary adsorption capacity, respectively.

Table 4
Pore structure parameters derived from LTNA/D.

Types	Sample	Pore structure parameters at different RH						
		0%	23%	33%	56%	75%	85%	98%
BET SSA, m^2/g	A1-1	30.51	6.90	5.78	3.02	2.01	1.21	0.82
	A1-2	36.38	8.55	7.20	4.07	3.06	1.91	1.33
	A1-3	27.74	5.93	5.16	2.64	1.57	0.90	0.65
	A1-4	22.47	5.80	4.99	3.18	2.25	1.14	0.83
	A1-5	27.79	6.02	5.20	2.61	1.56	1.08	0.77
	A1-6	34.19	7.50	6.30	2.67	1.92	1.38	0.71
	A1-7	33.27	7.72	7.14	5.37	4.58	3.54	3.22
Pore volume, 10^{-3} cm^3/g	A1-1	40.03	23.13	21.57	14.00	10.44	6.99	4.58
	A1-2	42.49	27.57	25.71	17.57	14.32	9.03	7.00
	A1-3	36.55	20.97	19.22	12.65	8.24	5.56	4.44
	A1-4	32.97	22.07	21.45	16.41	12.76	6.68	5.05
	A1-5	37.56	22.28	20.68	13.18	9.11	6.79	4.74
	A1-6	41.94	25.38	23.84	13.79	11.73	9.82	5.07
	A1-7	45.91	32.76	31.61	27.75	23.83	20.32	18.95
Average pore diameter, nm	A1-1	5.25	13.40	14.92	18.54	20.77	23.08	22.34
	A1-2	4.67	12.90	14.28	17.27	18.71	18.96	21.01
	A1-3	5.27	14.13	14.89	19.18	20.95	24.74	27.23
	A1-4	5.87	15.23	17.18	20.64	22.68	23.38	24.31
	A1-5	5.41	14.81	15.90	20.18	23.40	25.23	24.57
	A1-6	4.91	13.53	15.15	20.69	24.42	28.47	28.50
	A1-7	5.52	16.97	17.70	20.68	20.84	22.95	23.51

Table 5
Heterogeneity of PSD parameters derived from LTNA/D.

Types	Sample	Heterogeneity of PSD at different RH						
		0%	23%	33%	56%	75%	85%	98%
$D_{-10}-D_0$	A1-1	0.7499	0.4134	0.3971	0.3357	0.2877	0.3050	0.3005
	A1-2	0.7339	0.3790	0.3621	0.3237	0.2818	0.2561	0.2438
	A1-3	0.7773	0.4020	0.3945	0.2843	0.2669	0.2722	0.1775
	A1-4	0.7686	0.4187	0.3781	0.3357	0.2838	0.3246	0.3017
	A1-5	0.7764	0.4114	0.4050	0.3052	0.2883	0.2954	0.2928
	A1-6	0.7589	0.4028	0.4489	0.3115	0.2803	0.2765	0.1749
	A1-7	0.7177	0.3522	0.3422	0.3059	0.2895	0.2410	0.2653
D_0-D_{10}	A1-1	0.7643	0.8797	0.8875	0.9253	0.9327	0.9389	0.9358
	A1-2	0.7279	0.8785	0.8940	0.9160	0.9234	0.9123	0.9297
	A1-3	0.7669	0.8863	0.8938	0.9248	0.9342	0.9323	0.9391
	A1-4	0.7994	0.8969	0.9179	0.9277	0.9348	0.9342	0.9485
	A1-5	0.7747	0.8881	0.8990	0.9223	0.9363	0.9421	0.9518
	A1-6	0.7368	0.8808	0.8921	0.9333	0.9424	0.9525	0.9476
	A1-7	0.7861	0.9180	0.9236	0.9365	0.9393	0.9439	0.9475
$D_{-10}-D_{10}$	A1-1	1.5142	1.2931	1.2846	1.2610	1.2204	1.2439	1.2362
	A1-2	1.4618	1.2575	1.2561	1.2397	1.2053	1.1684	1.1735
	A1-3	1.5442	1.2884	1.2883	1.2091	1.2011	1.2045	1.1167
	A1-4	1.5142	1.2931	1.2846	1.2610	1.2204	1.2439	1.2362
	A1-5	1.5142	1.2931	1.2846	1.2610	1.2204	1.2439	1.2362
	A1-6	1.4956	1.2836	1.3410	1.2449	1.2227	1.2290	1.1225
	A1-7	1.5038	1.2702	1.2658	1.2423	1.2288	1.1849	1.2128

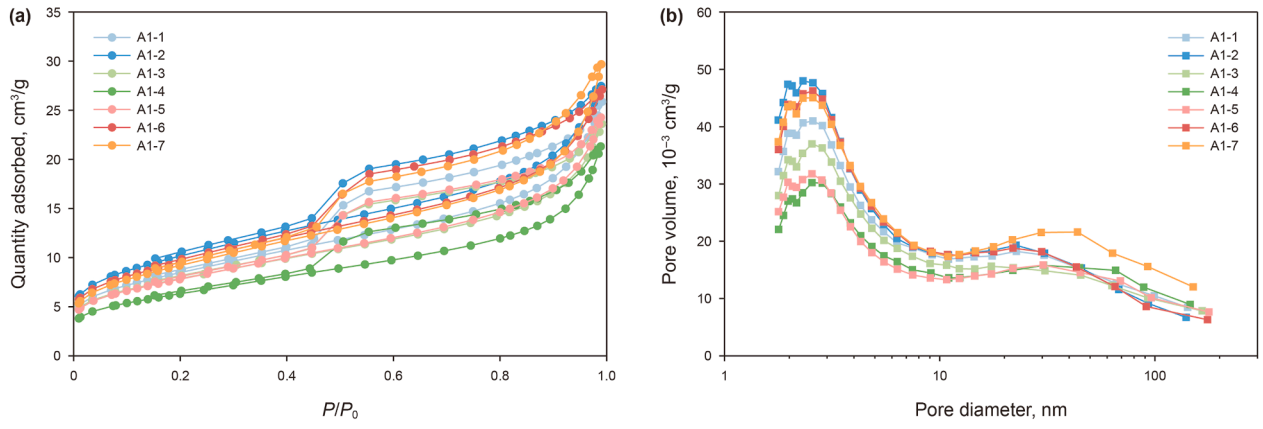


Fig. 5. LTNA/D isotherms **(a)** and PSDs **(b)** of original shale samples.

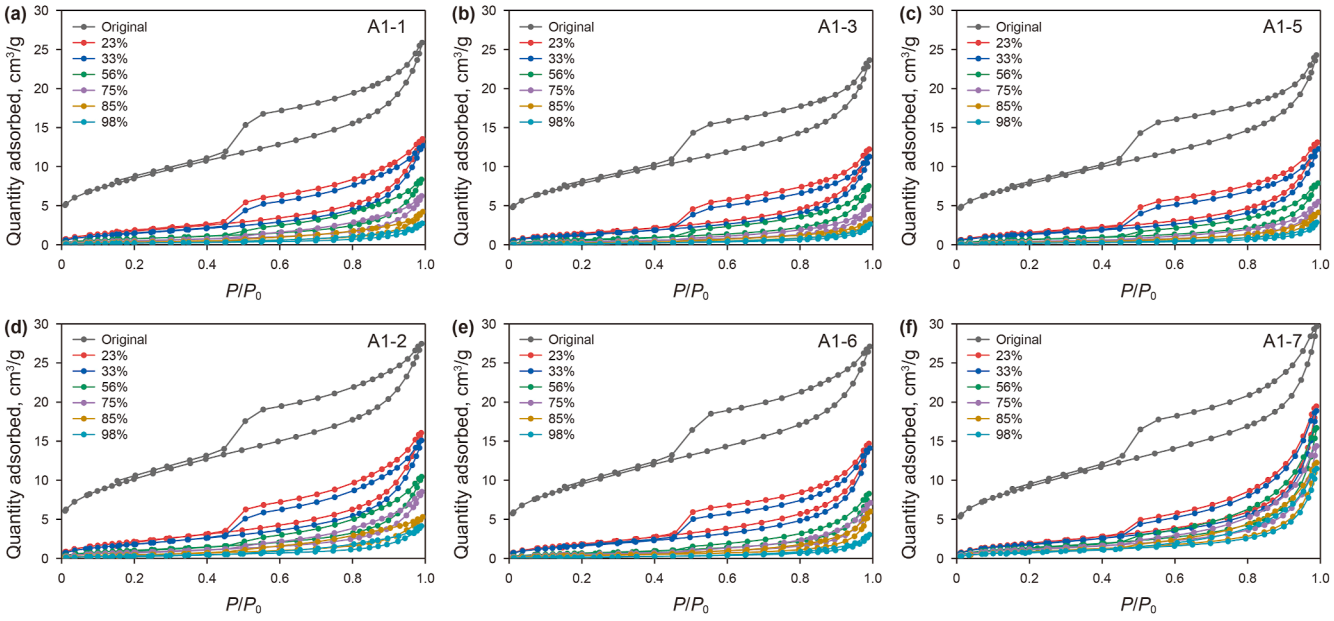


Fig. 6. LTNA/D isotherms of selected shales under different RH.

observations are consistent with the PSD: at early RH stages (below 23%), a marked reduction in micropore volume is detected. As RH increases beyond 56%, a further decrease in micropore content is evident, along with a concomitant reduction in macropore contribution. Consequently, the PSD evolves into a unimodal pattern dominated by the broader right-side peak (Fig. 7).

The PSDs of shales under different RH are shown in Fig. 7. Initially, all samples exhibit a bimodal distribution dominated by micropores. As RH increases to 23%, a sharp reduction in micropore volume is observed, suggesting that water vapor rapidly occupies the confined spaces within these small pores. In contrast, macropores remain largely unaffected, indicating that at this stage, water vapor adsorption occurs primarily on the internal surfaces of macropores, while their internal voids contain relatively few water molecules. With further increase in RH to 56%, a decreasing trend in macropore volume becomes evident, implying that only under higher humidity conditions does water vapor begin to significantly affect macropore interiors. Notably, beyond 56% RH, the rate of micropore volume reduction becomes negligible, suggesting that micropores are nearly saturated with water vapor at low to moderate RH. Despite continuous RH increases, the limited pore space within micropores restricts further adsorption. In contrast, mesopores and macropores display a gradual reduction in volume at intermediate to high RH, reflecting the progressive filling of internal voids by water vapor. At 98% RH, most samples exhibit nearly complete pore saturation. However, some exceptions remain, such as sample A1-7, which was not fully saturated (Fig. 7(f)). This anomaly may be attributed to its relatively high organic matter content (up to 3.2%), which may inhibit water vapor adsorption due to surface effects (Li et al., 2018; Chen et al., 2019).

LTNA/D experiments were employed to characterize the pore structure parameters of shale under varying RH conditions. Although slight variations exist among different samples, a general trend is observed: as RH increases, both the BET SSA and total PV consistently decrease, while the average pore diameter (APD) exhibits an increasing trend (Table 4 and Fig. 8). These observations indicate that water vapor preferentially adsorbs within smaller pores, leading to a reduction in accessible pore space and, consequently, a decline in both BET SSA and PV. This reduction is particularly pronounced between 23% and 33% RH, after which the rate of decrease becomes more gradual. In contrast, the APD shows an overall increase with rising RH. This apparent paradox can be attributed to the differential filling behavior of pores: micropores are rapidly occupied by water molecules, while larger pores are filled more slowly. As a result, despite the overall reduction in PV, the proportion of unfilled larger pores increases, thus raising the APD. This effect is most significant under low RH (<33%), beyond which the rate of change diminishes, suggesting that micropores become nearly saturated at low humidity, and subsequent water vapor adsorption occurs primarily within meso- and macropores.

4.3.3. Changes in shale multifractal characteristics

The multifractal characteristics of nitrogen adsorption data under varying RH conditions were systematically evaluated. A detailed analysis of the multifractal spectrum $q \sim D(q)$ was conducted, with key parameters including D_{-10}, D_{10}, D_0, D_0-D_{10}, $D_{-10}-D_0$, and $D_{-10}-D_{10}$ (Table 5). Among these, the left branch width ($D_{-10}-D_0$) and right branch width (D_0-D_{10}) are indicative of pore size heterogeneity within different PV regions (Fig. 9). Specifically, a larger $D_{-10}-D_0$ suggests greater heterogeneity in regions dominated by low PV, whereas a higher D_0-D_{10} reflects increased heterogeneity in regions characterized by high PV (Liu et al., 2018; Hou et al., 2020; Yao et al., 2024). In this study, the LTNA/D-derived PSD results for shales at RH exceeding 23% indicate that the fractal dimension $D_{-10}-D_0$ corresponds to the micropore domain, whereas D_0-D_{10} represents the macropore domain.

As RH increases, the value of $D_{-10}-D_0$ exhibits a decreasing trend, consistent with the variation pattern of $D_{-10}-D_{10}$, suggesting that the heterogeneity in the low PV region predominantly governs the overall pore structure heterogeneity. This observation further indicates that water vapor preferentially adsorbs and saturates the micropores during the initial stages of adsorption, exerting a more pronounced impact on this pore size domain. For

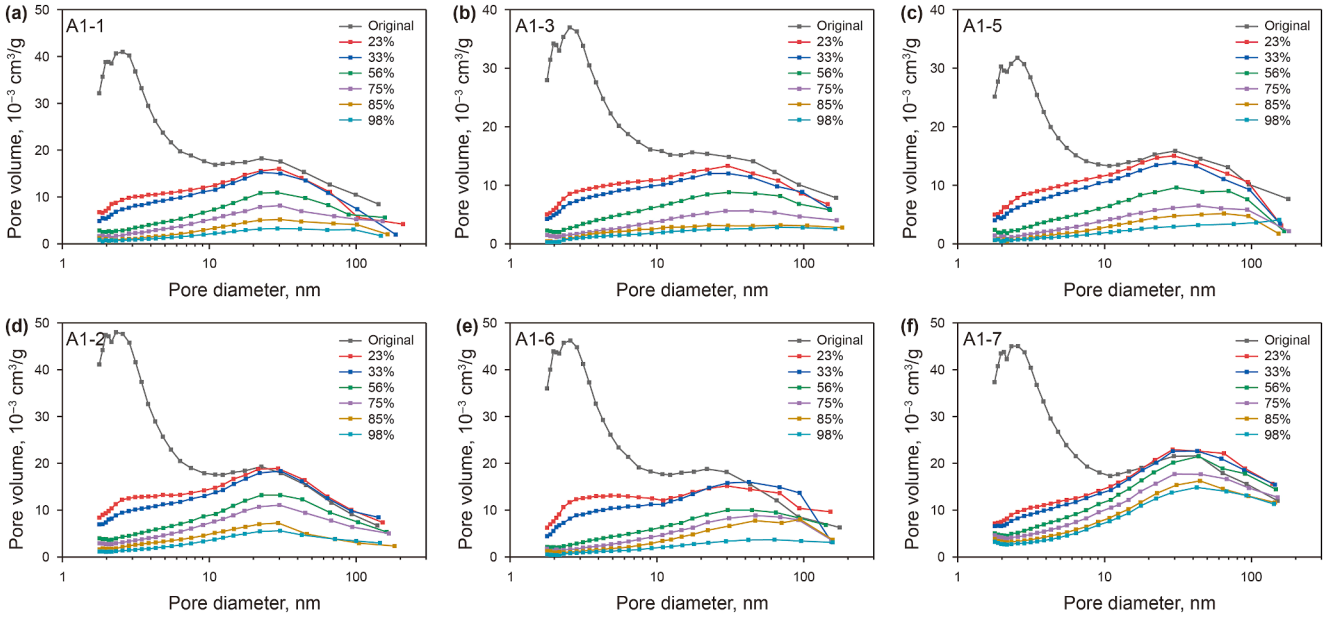


Fig. 7. Pore size distributions of selected shales under different RH.

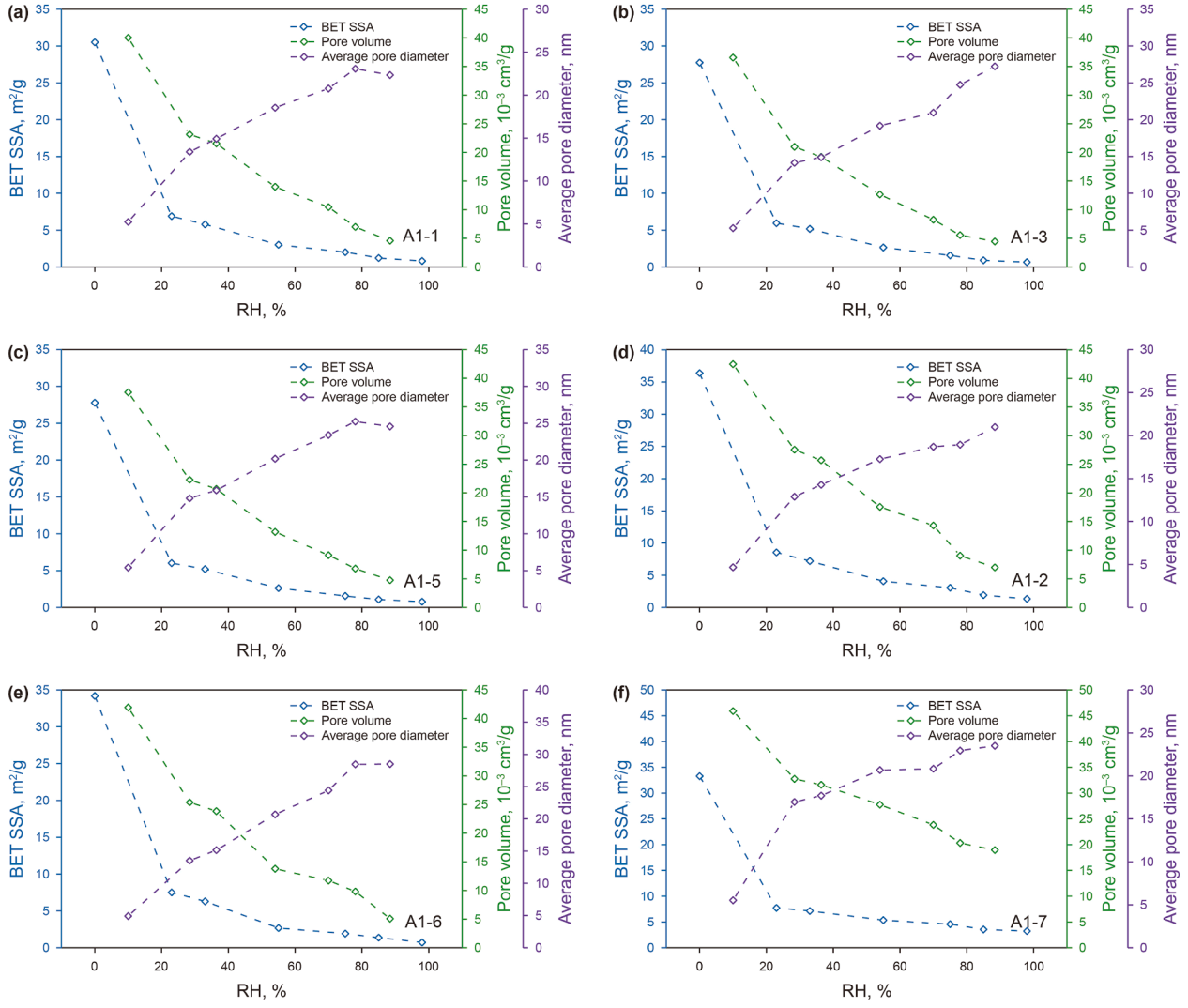


Fig. 8. Nitrogen adsorption pore structure parameters with RH variation.

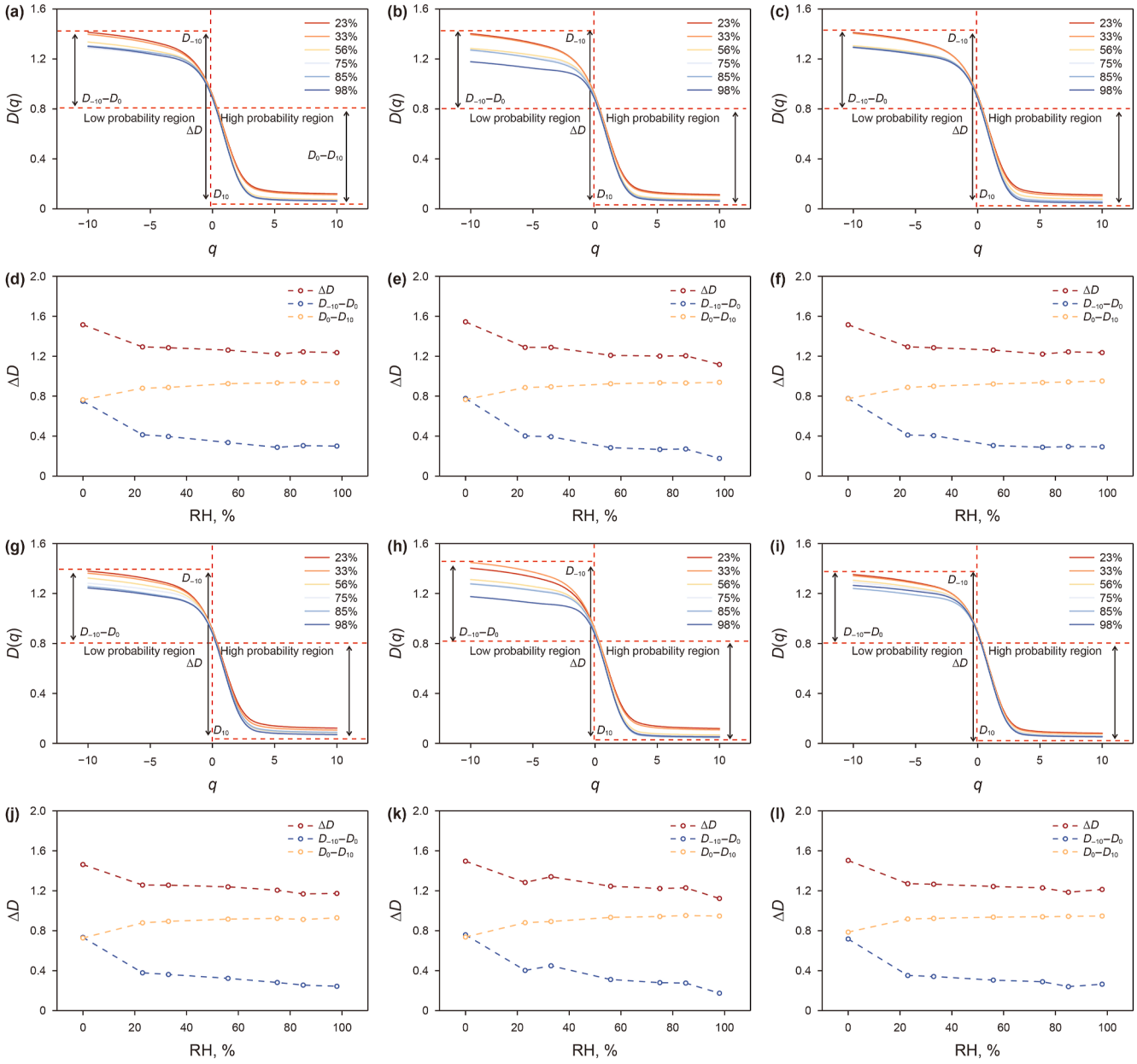


Fig. 9. Heterogeneity of PSD at different RH. **(a–c)** and **(g–i)** represent multifractal characteristics of different samples at different RH; **(d–f)** and **(j–l)** represent multifractal dimensions of different samples at different RH.

most samples, the pore structure heterogeneity reaches a relatively stable state when RH exceeds 56%. However, exceptions are observed in samples A1-3 and A1-6, where a continued reduction in heterogeneity is detected under high RH (98%). This may be attributed to the complex pore networks within these samples, where micropores that remained unsaturated at lower RH become progressively saturated as RH increases (Fig. 9(e) and (k)). Notably, the D_0-D_{10} representing the heterogeneity in the high PV region exhibits an opposite trend, showing a gradual increase with rising RH. This is likely due to the preferential filling of micropores, with limited influence on macropores. Additionally, under high RH, capillary-condensed water in macropores is not uniformly distributed and tends to form liquid bridges at specific pore throats, which disrupts pore connectivity and leads to a more discrete and heterogeneous distribution among macropores (Horikawa et al., 2015; Li et al., 2016a; Xie et al., 2023).

5. Discussion

5.1. Effect of minerals and TOC on pore structure and water adsorption

The IUPAC pore classification was applied to quantify BET SSA and PV for micropore (<2 nm), mesopore (2–50 nm), and macropore (>50 nm) size fractions in this study. These measurements were used to assess the influence of mineral compositions at different size scales on pore structure. The selected shales are dominated by quartz, feldspar, and clay minerals. The mineralogical composition exerts a primary control on pore-network development (Zhang et al., 2022; Wang et al., 2024b; Gao et al., 2025), and variations in pore architecture have been shown to influence water vapor adsorption. The K_2qn in the Gulong Sag exhibits relatively high thermal maturity, with most shales having

entered the late diagenetic stage. During diagenesis, acidic pore fluids became concentrated, promoting the dissolution of feldspar; specifically, K-feldspar was preferentially dissolved, releasing potassium ions that facilitated the transformation from smectite to illite (Jiang et al., 2025). This diagenetic process accounts for the near absence of K-feldspar and the predominance of plagioclase in the study area, and is consistent with the strong negative correlation between feldspar and clay mineral contents (Fig. 10(a)). Clay minerals constitute a major component of the shales, with illite as the predominant species. The presence of interlayer slit-like pores significantly increases the BET SSA and provides effective adsorption space (Zolfaghari et al., 2017a; Gao et al., 2022). Quartz grains are present as a rigid framework within the pore system and are largely resistant to acidic alteration. The relationships between clay minerals, quartz, and the pore network are therefore the primary focus of this study.

Micro- and mesopores are strongly correlated with the clay mineral content, indicating that clay minerals are the principal contributors to micro-scale pores (Fig. 10(c)). In contrast, quartz shows a stronger correlation with macropore, suggesting that quartz primarily contributes to larger pores (Fig. 10(d)). SEM images reveal that, although quartz grains are abundant, they generally occur as isolated particles dispersed within the matrix and are frequently cemented by clay minerals, resulting in limited pore development around grain boundaries (Fig. 3(a) and (c)). The relationship between TOC and pore structure is broadly similar to that of the clay fraction, with both exhibiting a strong positive correlation with each other (Fig. 10(a)). This similarity is attributed to the widespread occurrence of nano organo-clay complex pore-fractures in the K_2qn, which together constitute the principal storage space of these shales (Sun et al., 2024).

Clay minerals are widely regarded as one of the principal controls on the water vapor adsorption capacity of shales (Wang et al., 2019a; Chen et al., 2021a). At low RH, they exhibit strong positive correlations with both primary and secondary adsorption capacities (Fig. 11(a) and (b)), with intraparticle pores in clay minerals serving as the primary sites for adsorption (Zolfaghari et al., 2017a, 2017b). The correlation between clay mineral content and adsorption capacity decreases under higher RH, indicating that most micropores are nearly saturated with water molecules, leaving little additional space for further adsorption. However, there was no significant correlation between the quartz mineral content and the adsorption capacity (Fig. 11(c) and (d)). In general, mineral composition is not the sole factor controlling the water vapor adsorption capacity of shale. This variability may be attributed to differences in TOC content, PSD, and the SSA of the mineral framework (Xu et al., 2022; Xie et al., 2023).

Differences have been observed between lacustrine and marine shales regarding the influence of TOC on water vapor adsorption capacity. In the marine Longmaxi Formation shale, which is characterized by well-developed organic matter-hosted pores, a positive correlation between TOC and water vapor adsorption is observed. Moreover, the primary adsorption stage exhibits a better fitting accuracy than the secondary stage (Xu et al., 2022; Xie et al., 2023), suggesting that oxygen-containing functional groups in organic matter contribute substantially to water uptake and function as key adsorption sites in this reservoir type (Guo et al., 2018). In contrast, the correlation between TOC and adsorption capacity is less pronounced in the present study. The relationship between TOC and adsorption under varying RH more closely resembles that between clay mineral and adsorption capacity (Fig. 12(a) and (b)), which can be attributed to the organo-clay

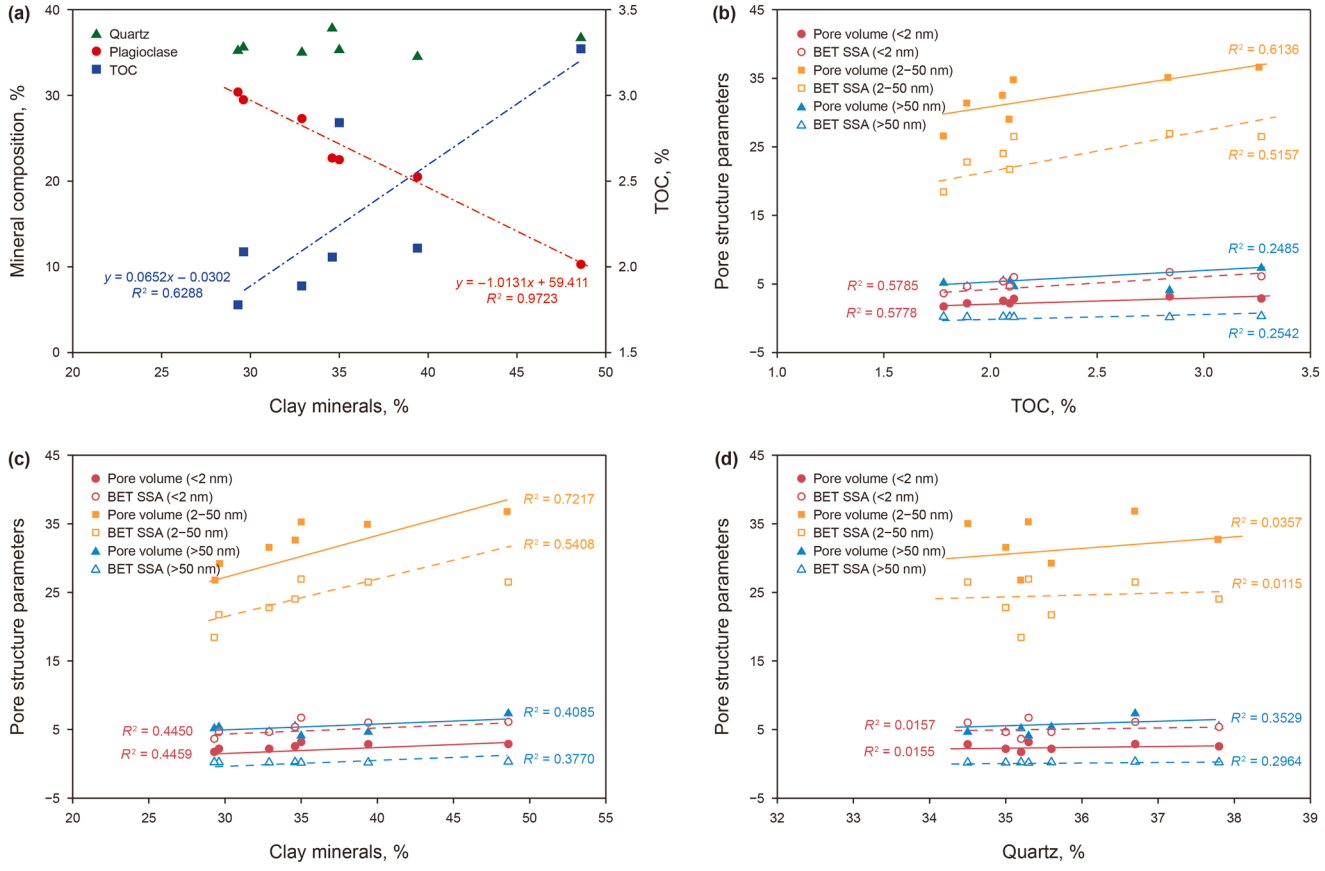


Fig. 10. Relationships between clay minerals and material compositions **(a)**; correlation between pore structure parameters and TOC **(b)**, and mineral composition **(c and d)**.

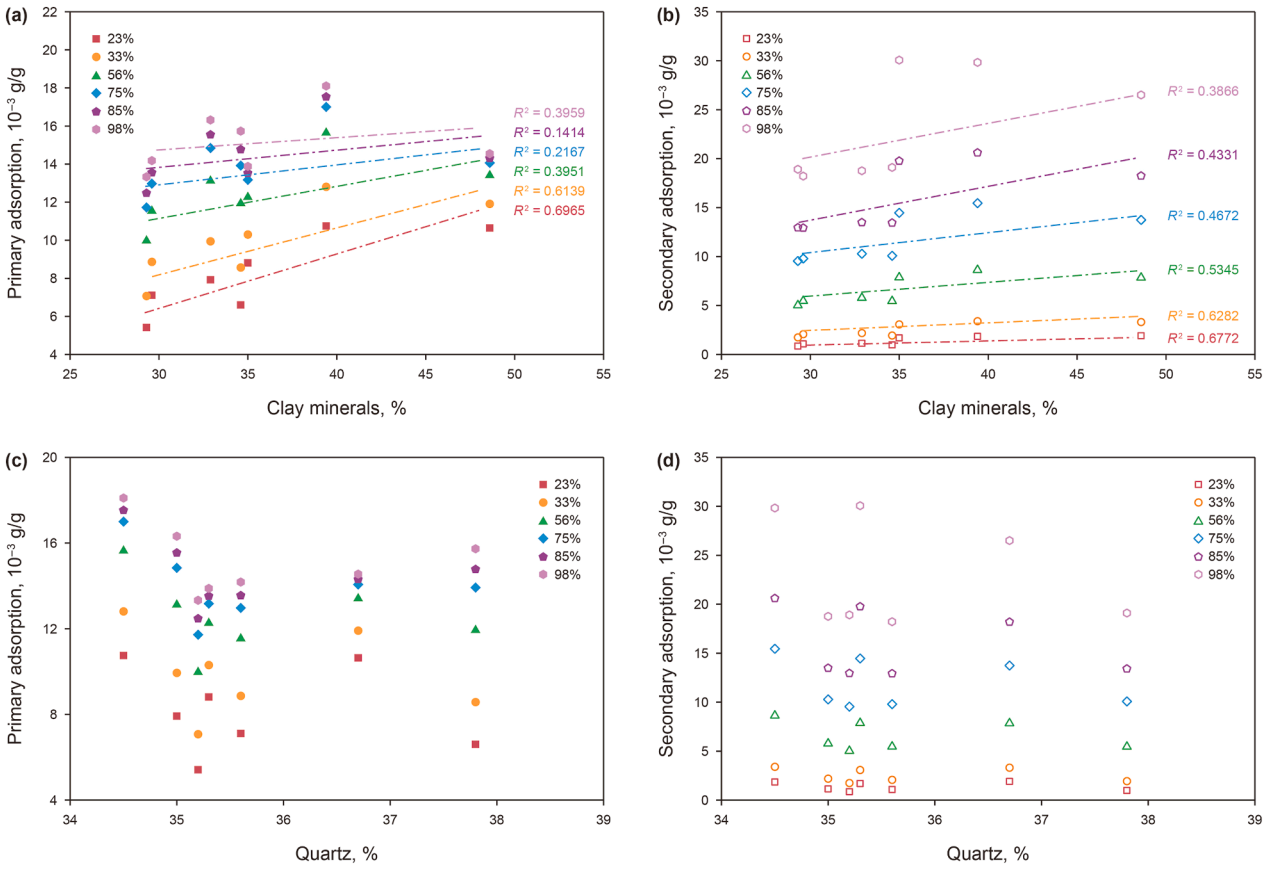


Fig. 11. Relationships between mineral composition and water vapor adsorption capacity under different RH.

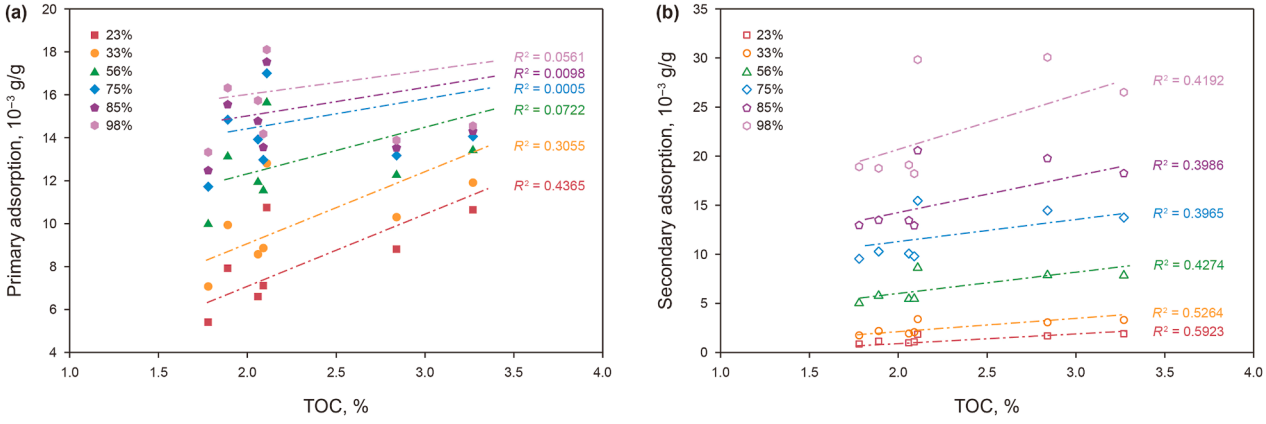


Fig. 12. Relationships between TOC and water vapor adsorption capacity under different RH.

complex pore-fractures of organic matter and clay minerals (Fig. 10(a)). Furthermore, TOC consistently shows weaker correlations with adsorption than clay mineral content under different RH, indicating that clay minerals represent the principal control on water vapor adsorption in these samples.

5.2. Effect of pore structure on water vapor adsorption

Variations in mineral composition within shale reservoirs are reflected in pore-network characteristics, which constitute a principal control on water vapor adsorption (Bai et al., 2020; Xie et al., 2023). Pore-structure parameters have been shown to strongly influence both primary and secondary water vapor adsorption in shales, particularly through the distinct roles of different pore-size ranges (Zou et al., 2020; Xu et al., 2022; Xie et al., 2023).

5.2.1. Effect of pore volume

Since LTNA/D experiments conducted at different RH provide measurements of the residual PV after water vapor adsorption, the PV measured at each RH was subtracted from that of the original (dry) state to determine the absolute PV occupied by water vapor at different RH. This approach enables an accurate evaluation of the impact of water vapor adsorption on PVs across different size

scales. Negative values of the macropore volume difference were observed for a subset of samples at low RH, which is attributed to pore-structure heterogeneity. This behavior is apparent in the PSDs derived from LTNA/D (Fig. 7(e) and (f)).

The contributions of pores of different size ranges to primary and secondary water vapor adsorption vary significantly. Primary adsorption exhibits a relatively steep slope and strong correlation with micropore volume at low RH (Fig. 13(a)). In comparison, secondary adsorption also correlates well with micropore volume but displays a lower magnitude and slope, indicating that water vapor preferentially and rapidly fills micropores through primary adsorption (Fig. 13(b)). As RH increases, both the correlation and slope for primary adsorption in micropores decrease, suggesting that most primary adsorption sites on pore surfaces are nearly saturated. In contrast, the slope for secondary adsorption in micropores increases, while the correlation remains consistently strong, implying that water vapor progressively occupies the internal space of micropores at high RH (Fig. 13(a) and (b)). Mesopores exhibit a different trend from micropores. At low RH (RH<33%), the adsorption capacity shows a relatively steep slope with respect to mesopore volume. With further increases in RH, primary adsorption sites in mesopores become gradually saturated, following a similar pattern to that in micropores but with higher slopes, suggesting that water vapor adsorption is dominated by mesopores under medium-to-high RH (Fig. 13(c) and (d)). However, the differences in capillary condensation within macropore systems typically render them unfavorable for water vapor adsorption (Fig. 13(e) and (f)) (Li et al., 2016a; Xie et al., 2023).

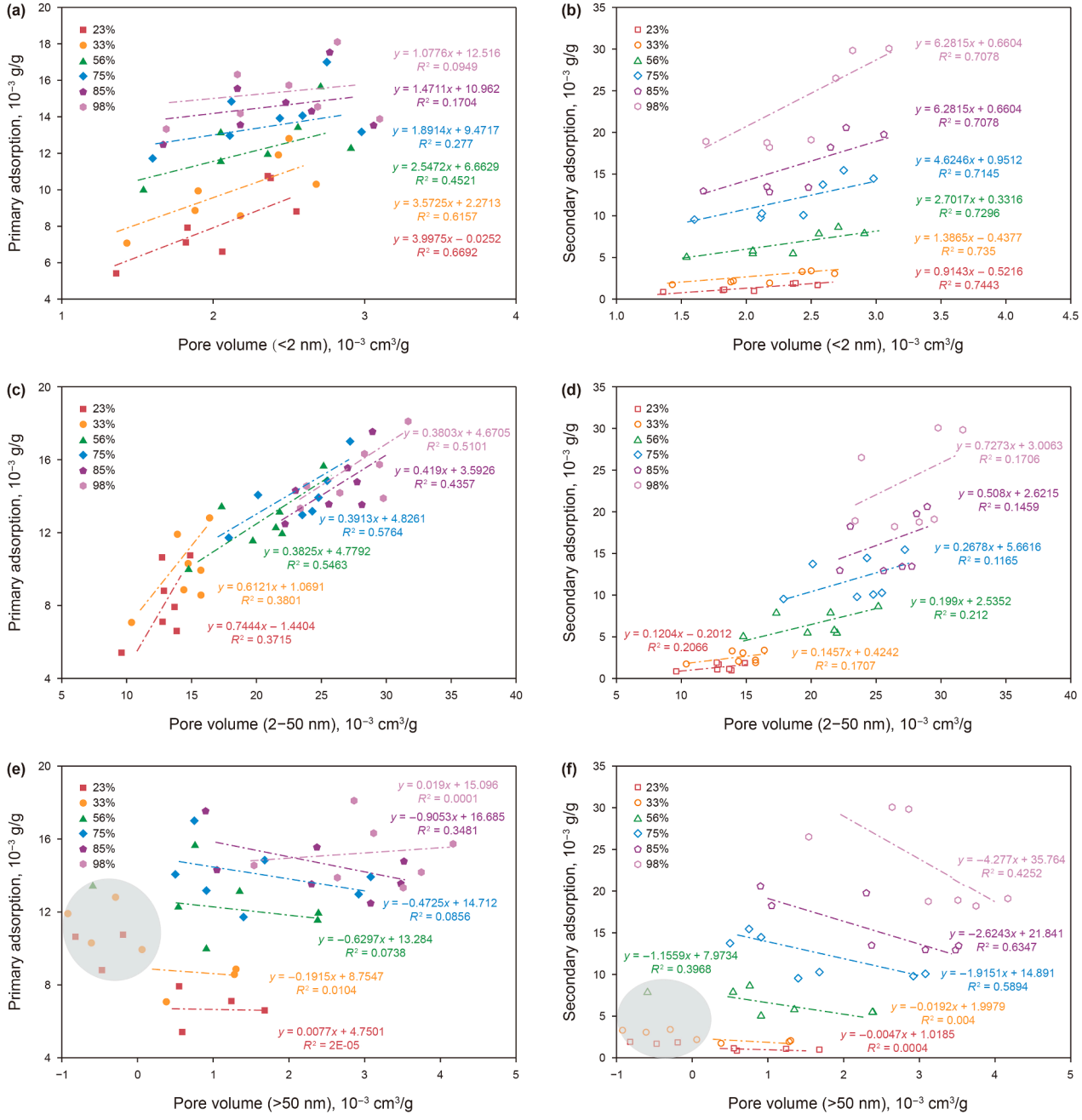


Fig. 13. Relationships between pore volume and water vapor adsorption capacity under different RH.

5.2.2. Effect of specific surface area

A gradual decrease in BET SSA was observed with increasing water vapor adsorption. Direct subtraction of SSA values under different RH may not accurately represent the extent of pore surface affected by adsorption. Accordingly, the following analysis is limited to the relationship between initial BET SSA and water vapor uptake under varying RH conditions.

SSA represents the dominant contributor to adsorption sites in shale, particularly primary adsorption sites, and has been shown to significantly affect primary adsorption capacity (Zeng et al., 2020; Chen et al., 2021b). Overall, the relationship between BET SSA and adsorption exhibits a trend similar to that of PV, while showing a higher goodness of fit. However, deviations are observed when compared to marine Longmaxi shale, likely due to differences in thermal maturity and TOC content, which directly influence pore system development (Mastalerz et al., 2013; Wang et al., 2020).

The influence of BET SSA on water vapor adsorption varies significantly across different pore size ranges. Correlations are notably higher in mesopores than in micropores, which may be attributed to the larger proportion of BET SSA contributed by mesopores. For both micropores and mesopores, the correlation between BET SSA and primary adsorption diminishes with increasing RH, likely due to the progressive occupation and depletion of primary adsorption sites. In contrast, secondary adsorption retains relatively high correlations with BET SSA in micropores and mesopores despite a declining trend, as it involves multilayer adsorption beyond the primary adsorption sites, including the onset of capillary condensation. Consequently,

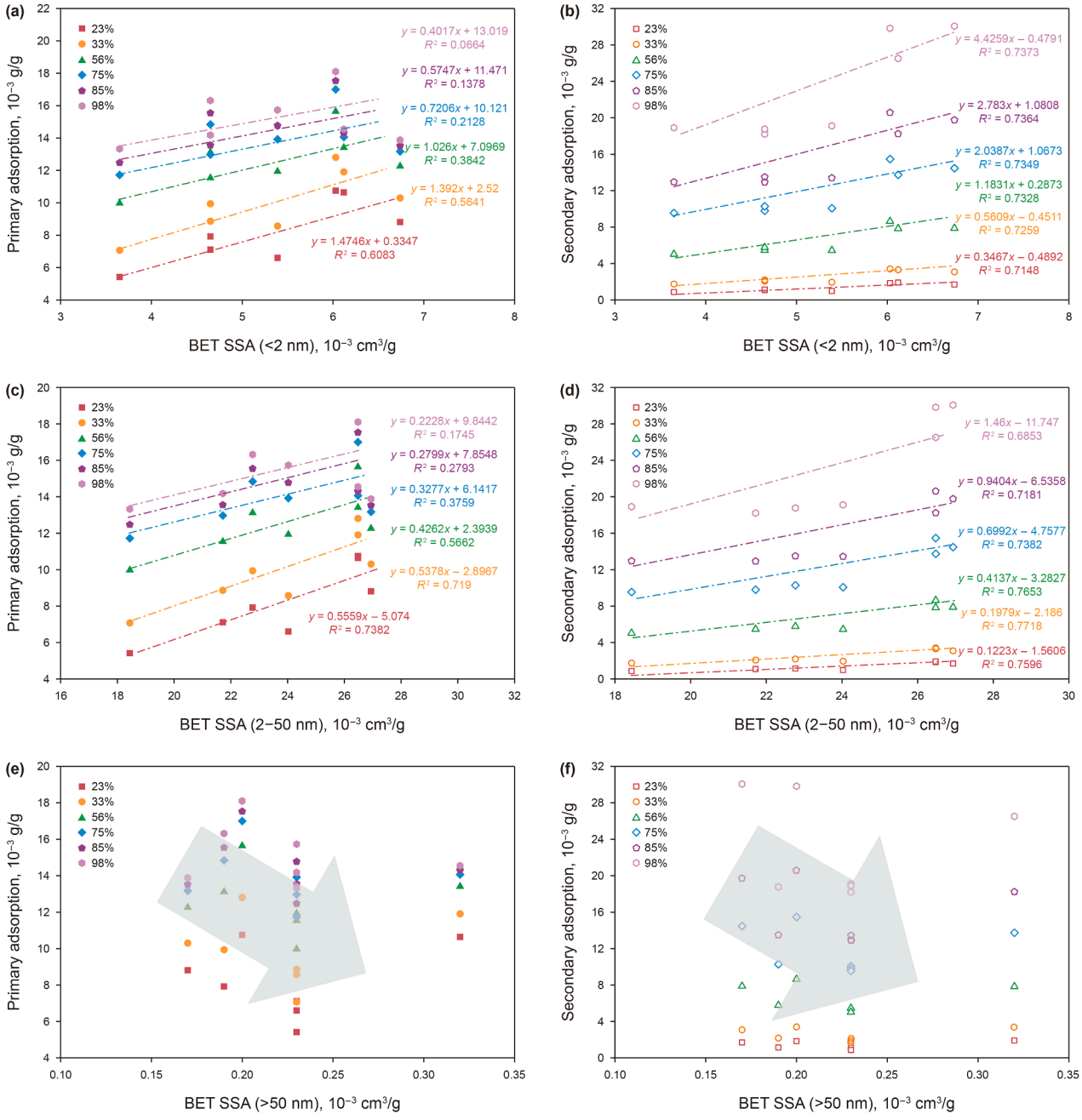


Fig. 14. Relationships between BET SSA and water vapor adsorption capacity under different RH.

secondary adsorption sites persist regardless of RH (Fig. 14(a)–(f)). In macropores, a generally negative correlation between SSA and water vapor adsorption is observed (Fig. 14(e) and (f)). This may be attributed to the dominance of quartz in large pore domains, whose surfaces are largely composed of hydrophobic siloxane groups, making them unfavorable for water vapor adsorption (Li et al., 2016a; Xie et al., 2023).

5.3. Effect of pore structure on heterogeneity

The analysis of pore heterogeneity evolution under varying RH provides valuable insights into the microscopic occurrence state and mobility of shale oil. Water vapor progressively occupies the pore spaces in shale samples with increasing RH, leading to the partial occlusion of previously accessible pore networks. This reduces the effective surface area and connectivity available for subsequent nitrogen adsorption, thereby affecting pore heterogeneity (Fig. 15). A consistent trend is observed between micro- and mesopore volume and the $D_{-10}-D_0$ under various RH (Fig. 15(a) and (b)). At low RH (<33%), a negative correlation is evident between micropore content and $D_{-10}-D_0$ across samples, indicating that greater micropore abundance is associated with a more uniform pore structure. This trend is attributed to the preferential filling of micropores by water vapor under low humidity conditions. Higher micropore content leads to a more uniform pore system after vapor adsorption, thereby reducing pore structural heterogeneity. However, when RH exceeds 56%, only minor changes in $D_{-10}-D_0$ are observed, indicating that water vapor adsorption primarily influences micropore heterogeneity at lower RH stages. Notably, significant variation is observed among samples. For instance, at 98% RH, several samples exhibit markedly low $D_{-10}-D_0$ values, implying that inter-sample differences are not limited to total pore volume, but may also involve differences in the three-dimensional spatial configuration of the pore networks (Feng et al., 2025).

As RH increases, the D_0-D_{10} exhibits an overall upward trend (Fig. 15(c)). However, the D_0-D_{10} decreases with increasing pore volume at each RH, and this decreasing trend becomes more pronounced at higher RH, indicating the influence of secondary adsorption at this stage. Notably, the observed deviation in sample A1-7 may be attributed to its exceptionally high TOC content. The relationship between macropore volume and the D_0-D_{10} is primarily evident under high RH (85% and 98%), whereas no clear correlation is observed at low RH. This suggests that capillary condensation in large pores significantly affects pore heterogeneity at high RH, and the non-uniform distribution of condensation among macropores further enhances heterogeneity, as reflected by higher D_0-D_{10} values in samples with more abundant macropores (Fig. 15(d)). Fundamentally, the variation in shale reservoir heterogeneity affects pore oil mobility, which in turn influences the production process. Specifically, such moisture-induced non-uniform filling is expected to enhance water blocking, potentially induce wettability alteration, and reduce oil mobility (Wang et al., 2019b; Xi et al., 2023).

5.4. Schematic diagram of pore water occurrence mode

Based on the preceding analysis of water vapor adsorption under different RH conditions, a schematic model of the adsorption process was developed (Fig. 16). SEM images indicate that

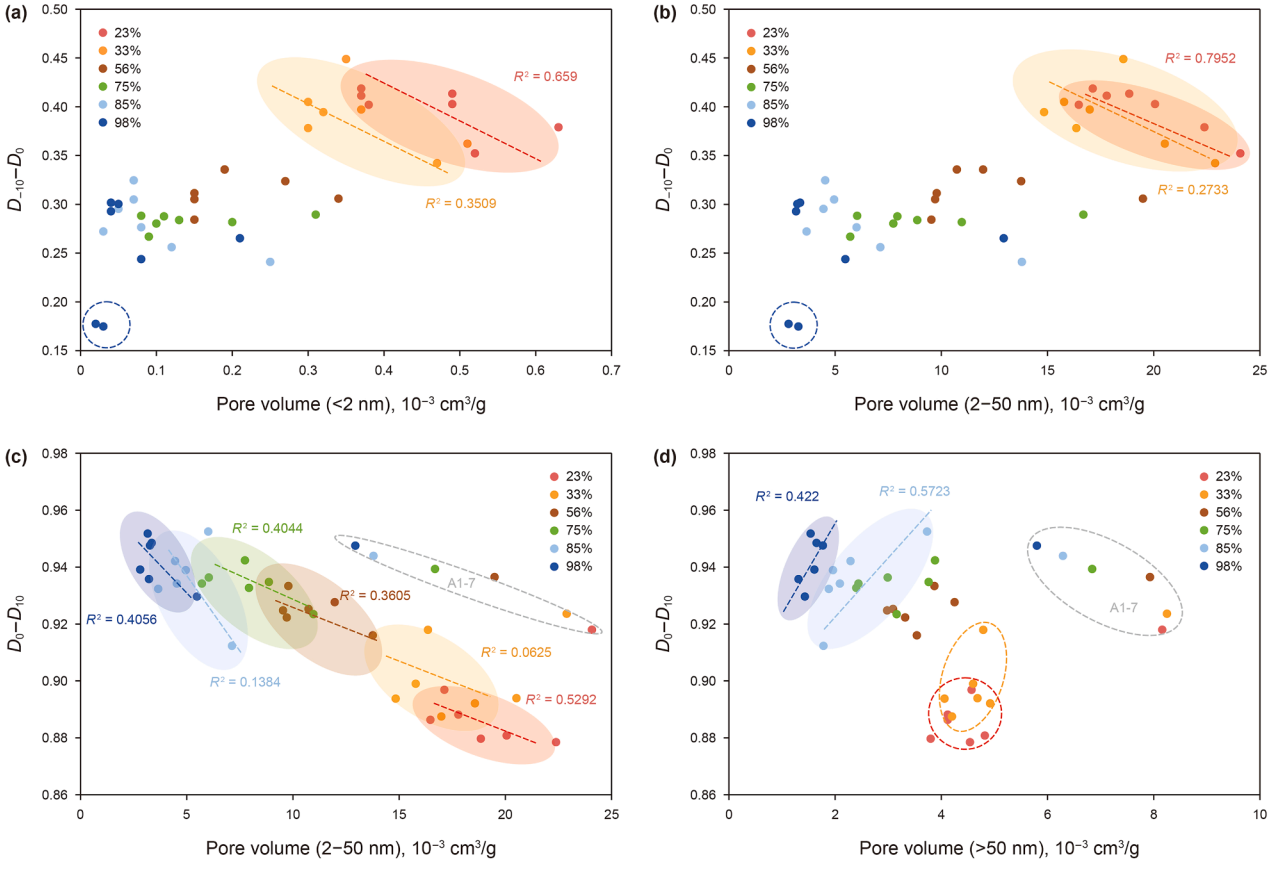


Fig. 15. Relationships between pore structure parameters and multifractal parameters under different RH.

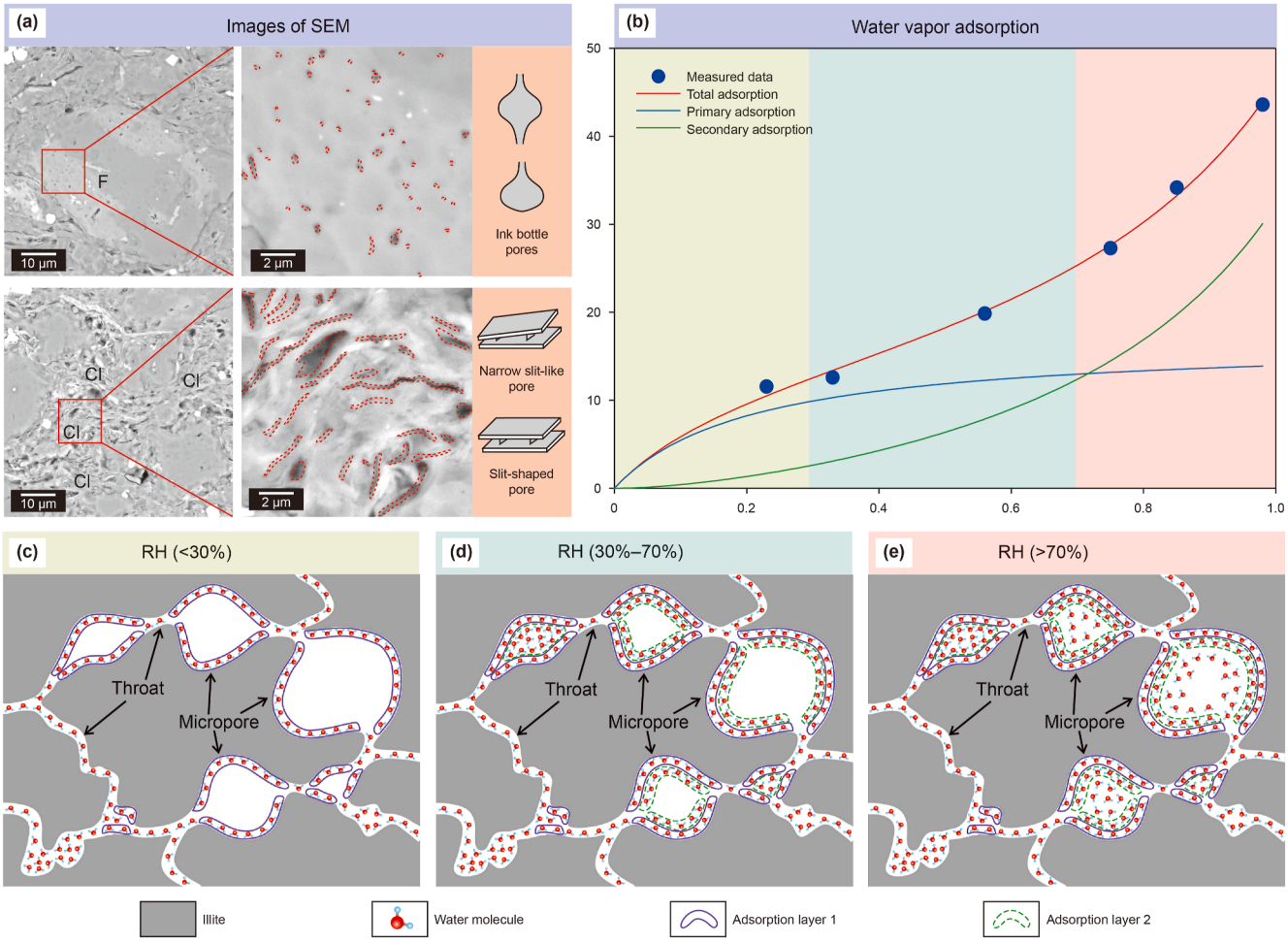


Fig. 16. Water vapor adsorption patterns for shale oil reservoirs.

shale in the study area predominantly contains ink-bottle and slit-shaped pores (Fig. 16(a)). Pores within clay minerals, particularly illite, which is the dominant clay component, provide a substantial number of adsorption sites for water molecules. Therefore, a pore water adsorption model was constructed based on illite-dominated pore structures.

The water vapor adsorption process can be broadly divided into three stages according to the morphology of the adsorption isotherms (Fig. 16(b)). For clarity, stage boundaries were approximated using integer RH values. The first stage is characterized by primary adsorption, in which water molecules are primarily adsorbed onto smaller pores via hydrogen bonding with surface hydroxyl groups or interlayer cations. This stage is dominated by physical adsorption, with limited secondary adsorption, and typically occurs at RH below 30% (Fig. 16(c)). The second stage occurs at RH values between 30% and 70%, during which primary adsorption becomes less significant while secondary adsorption gradually dominates. At this stage, most primary adsorption sites are occupied, and water molecules begin to adsorb in multilayers on pore surfaces (Fig. 16(d)). Capillary condensation may also occur in smaller pores during these two initial stages. The third stage, generally corresponding to RH above 70%, is dominated entirely by secondary adsorption. At this stage, primary adsorption is negligible, and water molecules form liquid bridges within pores, resulting in capillary condensation and the presence of bulk-like liquid water in meso- and macropores (Fig. 16(e)).

6. Conclusions

This study primarily focused on the description of the water vapor adsorption process and the factors affecting the primary and secondary adsorption contents, as well as the changes in pore structure heterogeneity during dynamic adsorption. The main conclusions are summarized as follows.

1) The Dent model provided an excellent fit to the water vapor adsorption data, allowing clear differentiation between primary adsorption at specific surface sites and secondary adsorption among water molecules. Primary adsorption followed a Type I isotherm, whereas secondary adsorption conformed to Type III.
2) Increasing RH led to a decrease in BET SSA and PV, while APD increased. The corresponding continuous decline in both ΔD and $D_{-10}-D_0$ suggests that pore structure heterogeneity is primarily governed by the low-value region of the pore size distribution. Under low RH, samples with higher micropore content tended to exhibit more homogeneous residual pore structures. In contrast, higher RH promoted capillary condensation in macropores, leading to increased D_0-D_{10} values due to the non-uniform condensation process.
3) Clay mineral content significantly influenced water vapor adsorption, particularly at low RH. Both SSA and PV showed a similar promoting effect, primarily within micro- and

mesopores, but their influence diminished as RH increased. In addition, macropores exhibited a negative correlation with total adsorption capacity, likely due to the suppression of capillary condensation in larger pores caused by size-dependent condensation thresholds.

4) A conceptual model was proposed for water vapor adsorption. At low RH (<30%), monolayer adsorption dominated, primarily on pore surfaces. In the intermediate range (30%–70%), multilayer adsorption prevailed as primary mechanisms weakened, especially on meso- and macropore surfaces. At high RH (>70%), secondary adsorption became dominant, characterized mainly by capillary condensation and liquid water formation in larger pores.

CRediT authorship contribution statement

Wei-Zheng Gao: Writing – original draft, Methodology, Investigation, Data curation, Conceptualization. **Peng-Fei Zhang:** Writing – review & editing, Methodology, Investigation, Funding acquisition. **Jun-Jie Wang:** Writing – review & editing, Investigation, Funding acquisition. **Hai-Yong Wang:** Writing – review & editing, Investigation. **Neng-Wu Zhou:** Writing – review & editing. **Wen-Biao Li:** Writing – review & editing. **Guo-Hui Chen:** Writing – review & editing. **Chen-Xi Wu:** Data curation. **Shuang-Fang Lu:** Writing – review & editing, Methodology, Investigation.

Conflict of interest statement

The authors declare that they have no known competing financial interests or personal relationships that could have appeared to influence the work reported in this paper.

Acknowledgments

This study was financially supported by the National Natural Science Foundation of China (42572168 and 42302160), the PhD Scientific Research and Innovation Foundation of the Education Department of Hainan Province Joint Project of Sanya Yazhou Bay Science and Technology City (HSPHDSRF-2024-07-001), and Research Startup Funding Project for Talent Introduction of Northeast Petroleum University (13051202402).

References

Bai, J., Kang, Y., Chen, M., et al., 2020. Impact of surface chemistry and pore structure on water vapor adsorption behavior in gas shale. Chem. Eng. J. 402, 126238. https://doi.org/10.1016/j.cej.2020.126238.

Brunauer, S., Emmett, P.H., Teller, E., 1938. Adsorption of gases in multimolecular layers. J. Am. Chem. Soc. 60 (2), 309–319. https://doi.org/10.1021/ja01269a023.

Charrière, D., Behra, P., 2010. Water sorption on coals. J. Colloid Interface Sci. 344 (2), 460–467. https://doi.org/10.1016/j.jcis.2009.11.064.

Chen, G., Li, C., Lu, S., et al., 2021a. Critical factors controlling adsorption capacity of shale gas in Wufeng–Longmaxi Formation, Sichuan Basin: evidences from both experiments and molecular simulations. J. Nat. Gas Sci. Eng. 88, 103774. https://doi.org/10.1016/j.jngse.2020.103774.

Chen, J., Gai, H., Xiao, Q., 2021b. Effects of composition and temperature on water sorption in overmature Wufeng–Longmaxi shales. Int. J. Coal Geol. 234, 103673. https://doi.org/10.1016/j.coal.2020.103673.

Chen, Z., Song, Y., Li, Z., et al., 2019. The occurrence characteristics and removal mechanism of residual water in marine shales: A case study of Wufeng–Longmaxi shale in Changning-Weiyuan area, Sichuan Basin. Fuel 253, 1056–1070. https://doi.org/10.1016/j.fuel.2019.05.069.

Cheng, P., Xiao, X., Wang, X., et al., 2019. Evolution of water content in organic-rich shales with increasing maturity and its controlling factors: Implications from a pyrolysis experiment on a water-saturated shale core sample. Mar. Petrol. Geol. 109, 291–303. https://doi.org/10.1016/j.marpetgeo.2019.06.023.

Dang, W., Jiang, S., Zhang, J., et al., 2021. A systematic experimental and modeling study of water adsorption/desorption behavior in organic-rich shale with different particle sizes. Chem. Eng. J. 426, 130596. https://doi.org/10.1016/j.cej.2021.130596.

Dent, R.W., 1977. A multilayer theory for gas sorption: Part I: S orption of a single gas. Textil. Res. J. 47 (2), 145–152. https://doi.org/10.1177/004051757704700213.

Dole, M., 1948. Statistical thermodynamics of the sorption of vapors by solids. J. Chem. Phys. 16 (1), 25–30. https://doi.org/10.1063/1.1746648.

Feng, D., Li, X., Wang, X., et al., 2018. Water adsorption and its impact on the pore structure characteristics of shale clay. Appl. Clay Sci. 155, 126–138. https://doi.org/10.1016/j.clay.2018.01.017.

Feng, G., Zhang, L., Yan, J., et al., 2025. Lithofacies-based analysis of pore structure characteristics and controlling factors of shale reservoirs: A case study of the second member of the Kongdian Formation in the Cangdong Sag, Bohai Bay Basin. China. Mar. Petrol. Geol. 182, 107575. https://doi.org/10.1016/j.marpetgeo.2025.107575.

Gao, W., Zhang, P., Wang, J., et al., 2025. Insights into shale pore structure and microscopic fluid occurrence characteristics in the Paleogene Funing Formation, Subei Basin. China. Mar. Petrol. Geol. 179, 107434. https://doi.org/10.1016/j.marpetgeo.2025.107434.

Gao, Z.Y., Xiong, S.L., Wei, L., 2022. The new multistage water adsorption model of Longmaxi Formation shale considering the spatial configuration relationship between organic matter and clay minerals. Petrol. Sci. 19 (5), 1950–1963. https://doi.org/10.1016/j.petsci.2022.05.014.

Guo, J., Zhang, L., Liu, S., et al., 2018. Effects of hydrophilic groups of nonionic surfactants on the wettability of lignite surface: Molecular dynamics simulation and experimental study. Fuel 231, 449–457. https://doi.org/10.1016/j.fuel.2018.05.106.

Hatch, C.D., Wiese, J.S., Crane, C.C., et al., 2012. Water adsorption on clay minerals as a function of relative humidity: Application of BET and Freundlich adsorption models. Langmuir 28 (3), 1790–1803. https://doi.org/10.1021/la2042873.

He, W.Y., Liu, B., Zhang, J.Y., et al., 2023. Geological characteristics and key scientific and technological problems of Gulong shale oil in Songliao Basin. Earth Sci. 48 (1), 49–62. https://doi.org/10.3799/dqkx.2022.320 (in Chinese).

Horikawa, T., Muguruma, T., Do, D.D., et al., 2015. Scanning curves of water adsorption on graphitized thermal carbon black and ordered mesoporous carbon. Carbon 95, 137–143. https://doi.org/10.1016/j.carbon.2015.08.034.

Hou, X., Zhu, Y., Chen, S., et al., 2020. Investigation on pore structure and multifractal of tight sandstone reservoirs in coal bearing strata using LF-NMR measurements. J. Petrol. Sci. Eng. 187, 106757. https://doi.org/10.1016/j.petrol.2019.106757.

Jia, J., Liu, Z., Bechtel, A., et al., 2013. Tectonic and climate control of oil shale deposition in the Upper Cretaceous Qingshankou Formation (Songliao Basin, NE China). Int. J. Earth Sci. 102 (6), 1717–1734. https://doi.org/10.1007/s00531-013-0903-7.

Jiang, X., Zhu, R., Wu, S., et al., 2025. Pore characteristics of clay minerals in the Qingshankou shale, Songliao Basin, China: Unravelling the effects of illitization. Front. Earth Sci. 13, 1524678. https://doi.org/10.3389/feart.2025.1524678.

Jin, Z., Zhu, R., Liang, X., et al., 2021. Several issues worthy of attention in current lacustrine shale oil exploration and development. Petrol. Explor. Dev. 48 (6), 1471–1484. https://doi.org/10.1016/S1876-3804(21)60303-8.

Korb, J.P., Nicot, B., Louis-Joseph, A., et al., 2014. Dynamics and wettability of oil and water in oil shales. J. Phys. Chem. C 118 (40), 23212–23218. https://doi.org/10.1021/jp508659e.

Lahn, L., Bertier, P., Seemann, T., et al., 2020. Distribution of sorbed water in the pore network of mudstones assessed from physisorption measurements. Microporous Mesoporous Mater. 295, 109902. https://doi.org/10.1016/j.micromeso.2019.109902.

Langmuir, I., 1918. The adsorption of gases on plane surfaces of glass, mica and platinum. J. Am. Chem. Soc. 40 (9), 1361–1403. https://doi.org/10.1021/ja02242a004.

Li, J., Chen, Z., Li, X., et al., 2018. A quantitative research of water distribution characteristics inside shale and clay nanopores. Sci. Sin.-Tech. 48 (11), 1219–1233. https://doi.org/10.1360/N092017-00137.

Li, J., Li, X., Wang, X., et al., 2016a. Water distribution characteristic and effect on methane adsorption capacity in shale clay. Int. J. Coal Geol. 159, 135–154. https://doi.org/10.1016/j.coal.2016.03.012.

Li, J., Li, X., Wu, K., et al., 2016b. Water sorption and distribution characteristics in clay and shale: effect of surface force. Energy Fuel. 30 (11), 8863–8874. https://doi.org/10.1021/acs.energyfuels.6b00927.

Li, J., Wang, S., Lu, S., et al., 2019. Microdistribution and mobility of water in gas shale: A theoretical and experimental study. Mar. Petrol. Geol. 102, 496–507. https://doi.org/10.1016/j.marpetgeo.2019.01.012.

Li, W., Wang, J., Jia, C., et al., 2024. Carbon isotope fractionation during methane transport through tight sedimentary rocks: Phenomena, mechanisms, characterization, and implications. Geosci. Front. 15 (6), 101912. https://doi.org/10.1016/j.gsf.2024.101912.

Liu, C., Wang, Z., Guo, Z., et al., 2017. Enrichment and distribution of shale oil in the Cretaceous Qingshankou Formation, Songliao Basin, Northeast China. Mar. Petrol. Geol. 86, 751–770. https://doi.org/10.1016/j.marpetgeo.2017.06.034.

Liu, K., Ostadhassan, M., Zou, J., et al., 2018. Multifractal analysis of gas adsorption isotherms for pore structure characterization of the Bakken Shale. Fuel 219, 296–311. https://doi.org/10.1016/j.fuel.2018.01.126.

Mastalerz, M., Schimmelmann, A., Drobniak, A., et al., 2013. Porosity of Devonian and Mississippian New Albany Shale across a maturation gradient: Insights from organic petrology, gas adsorption, and mercury intrusion. AAPG Bull. 97 (10), 1621–1643. https://doi.org/10.1306/04011312194.

Qin, X., Wu, J., Xia, Y., et al., 2024. Multicomponent image-based modeling of water flow in heterogeneous wet shale nanopores. Energy 298, 131367. https://doi.org/10.1016/j.energy.2024.131367.
Sang, G., Liu, S., Elsworth, D., 2019. Water vapor sorption properties of Illinois shales under dynamic water vapor conditions: Experimentation and modeling. Water Resour. Res. 55 (8), 7212–7228. https://doi.org/10.1029/2019wr024992.
Shen, W., Li, X., Lu, X., et al., 2018. Experimental study and isotherm models of water vapor adsorption in shale rocks. J. Nat. Gas Sci. Eng. 52, 484–491. https://doi.org/10.1016/j.jngse.2018.02.002.
Sulucarnain, I., Sondergeld, C.H., Rai, C.S., 2012. An NMR study of shale wettability and effective surface relaxivity. In: SPE Canadian Unconventional Resources Conference, Richardson. https://doi.org/10.2118/162236-ms.
Sun, L., Liu, H., He, W., et al., 2021. An analysis of major scientific problems and research paths of Gulong shale oil in Daqing Oilfield, NE China. Petrol. Explor. Dev. 48 (3), 527–540. https://doi.org/10.1016/S1876-3804(21)60043-5.
Sun, L., Wang, F., Bai, X., et al., 2024. Discovery of nano organo-clay complex pore-fractures in shale and its scientific significance: A case study of Cretaceous Qingshankou Formation shale, Songliao Basin, NE China. Petrol. Explor. Dev. 51 (4), 813–825. https://doi.org/10.1016/S1876-3804(24)60508-2.
Wang, C., Feng, Z., Zhang, L., et al., 2013. Cretaceous paleogeography and paleoclimate and the setting of SKI borehole sites in Songliao Basin, Northeast China. Palaeogeogr. Palaeoclimatol. Palaeoecol. 385, 17–30. https://doi.org/10.1016/j.palaeo.2012.01.030.
Wang, J., Lu, S., Zhang, P., et al., 2024b. Characterization of shale oil and water micro-occurrence based on a novel method for fluid identification by NMR T_2 spectrum. Fuel 374, 132426. https://doi.org/10.1016/j.fuel.2024.132426.
Wang, J., Wang, F., Chen, F., et al., 2024a. Dynamic fractionation of methane carbon isotope during mass transport in coal with bidisperse pore structures: experiments, numerical modeling, and applications. Chem. Eng. J. 498, 154942. https://doi.org/10.1016/j.cej.2024.154942.
Wang, J.J., Zhang, P.F., Lu, S.F., et al., 2025. Insights into microscopic oil occurrence characteristics in shales from the Paleogene Funing Formation in Subei Basin, China. Petrol. Sci. 22 (1), 55–75. https://doi.org/10.1016/j.petsci.2024.07.025.
Wang, M., Ma, R., Li, J., et al., 2019b. Occurrence mechanism of lacustrine shale oil in the Paleogene Shahejie Formation of Jiyang Depression, Bohai Bay Basin, China. Petrol. Explor. Dev. 46 (4), 833–846. https://doi.org/10.1016/S1876-3804(19)60242-9.
Wang, T., Tian, S., Li, G., et al., 2019a. Experimental study of water vapor adsorption behaviors on shale. Fuel 248, 168–177. https://doi.org/10.1016/j.fuel.2019.03.029.
Wang, Y., Liu, L., Hu, Q., et al., 2020. Nanoscale pore network evolution of Xiamaling marine shale during organic matter maturation by hydrous pyrolysis. Energy Fuel. 34 (2), 1548–1563. https://doi.org/10.1021/acs.energyfuels.9b03686.
Xi, K., Zhang, Y., Cao, Y., et al., 2023. Control of micro-wettability of pore-throat on shale oil occurrence: A case study of laminated shale of Permian Lucaogou Formation in Jimusar Sag, Junggar Basin, NW China. Petrol. Explor. Dev. 50 (2), 334–345. https://doi.org/10.1016/S1876-3804(23)60391-X.
Xie, W., Wang, H., Chen, S., et al., 2023. Water adsorption and its pore structure dependence in shale gas reservoirs. Langmuir 39 (30), 10576–10592. https://doi.org/10.1021/acs.langmuir.3c01159.
Xing, Y.J., Xiao, X.M., Cheng, P., et al., 2025. Water adsorption performance of over-mature shale and its relationship with organic and inorganic nanopores: A case study of Lower Cambrian shale from the Sichuan Basin, China. Petrol. Sci. 22 (3), 977–997. https://doi.org/10.1016/j.petsci.2024.12.025.
Xu, J., Bechtel, A., Sachsenhofer, R.F., et al., 2015. High resolution geochemical analysis of organic matter accumulation in the Qingshankou Formation, Upper Cretaceous, Songliao Basin (NE China). Int. J. Coal Geol. 141–142, 23–32. https://doi.org/10.1016/j.coal.2015.03.003.
Xu, L., Wei, H., Chen, L., et al., 2022. Storing characteristics and main controlling factors of connate water in lower Paleozoic shales in southeast Chongqing, China. J. Petrol. Sci. Eng. 215, 110543. https://doi.org/10.1016/j.petrol.2022.110543.
Yang, R., Jia, A., He, S., et al., 2020. Water adsorption characteristics of organic-rich Wufeng and Longmaxi Shales, Sichuan Basin (China). J. Petrol. Sci. Eng. 193, 107387. https://doi.org/10.1016/j.petrol.2020.107387.
Yao, P., Zhang, J., Lv, D., et al., 2024. Effect of water occurrence in coal reservoirs on the production capacity of coalbed methane by using NMR simulation technology and production capacity simulation. Geoenergy Sci. Eng. 243, 213353. https://doi.org/10.1016/j.geoen.2024.213353.
Zeng, T., Kim, K.T., Werth, C.J., et al., 2020. Surfactant adsorption on shale samples: Experiments and an additive model. Energy Fuel. 34 (5), 5436–5443. https://doi.org/10.1021/acs.energyfuels.9b04016.
Zhang, P., Lu, S., Li, J., 2019. Characterization of pore size distributions of shale oil reservoirs: A case study from Dongying sag, Bohai Bay Basin. China. Mar. Petrol. Geol. 100, 297–308. https://doi.org/10.1016/j.marpetgeo.2018.11.024.
Zhang, P., Yin, Y., Lu, S., et al., 2022. Insights into pore structures and multifractal characteristics of shale oil reservoirs: A case study from Dongying Sag, Bohai Bay Basin, China. Energy Fuel. 36 (15), 8224–8237. https://doi.org/10.1021/acs.energyfuels.2c01763.
Zhang, P.F., Lu, S.F., Wang, J.J., et al., 2024. Microscopic occurrence and distribution of oil and water in situ shale: Evidence from nuclear magnetic resonance. Petrol. Sci. 21 (6), 3675–3691. https://doi.org/10.1016/j.petsci.2024.04.007.
Zhang, P.F., Wang, J.J., Lu, S.F., et al., 2025. Insights into occurrence and distribution of pore water in gas shales: Comparison between thermogravimetry and water vapor sorption. Petrol. Sci. 22 (10), 3939–3959. https://doi.org/10.1016/j.petsci.2025.07.007.
Zhang, S., Zhang, B., Wang, X., et al., 2023. Gulong shale oil enrichment mechanism and orderly distribution of conventional–unconventional oils in the Cretaceous Qingshankou Formation, Songliao Basin, NE China. Petrol. Explor. Dev. 50 (5), 1045–1059. https://doi.org/10.1016/S1876-3804(23)60448-3.
Zolfaghari, A., Dehghanpour, H., Holyk, J., 2017a. Water sorption behaviour of gas shales: I. Role of clays. Int. J. Coal Geol. 179, 130–138. https://doi.org/10.1016/j.coal.2017.05.008.
Zolfaghari, A., Dehghanpour, H., Xu, M., 2017b. Water sorption behaviour of gas shales: II. Pore size distribution. Int. J. Coal Geol. 179, 187–195. https://doi.org/10.1016/j.coal.2017.05.009.
Zou, C., Zhu, R., Chen, Z.Q., et al., 2019. Organic-matter-rich shales of China. Earth Sci. Rev. 189, 51–78. https://doi.org/10.1016/j.earscirev.2018.12.002.
Zou, J., Rezaee, R., Yuan, Y., et al., 2020. Distribution of adsorbed water in shale: An experimental study on isolated kerogen and bulk shale samples. J. Petrol. Sci. Eng. 187, 106858. https://doi.org/10.1016/j.petrol.2019.106858.